

Stable nickel production in Type Ia supernovae: A smoking gun for the progenitor mass?

S. Blondin^{1,2}, E. Bravo³, F. X. Timmes^{4,5}, L. Dessart⁶, and D. J. Hillier⁷

¹ Aix Marseille Univ, CNRS, CNES, LAM, Marseille, France
e-mail: stephane.blondin@lam.fr

² Unidad Mixta Internacional Franco-Chilena de Astronomía, CNRS/INSU UMI 3386 and Instituto de Astrofísica, Pontificia Universidad Católica de Chile, Santiago, Chile

³ E.T.S. Arquitectura del Vallès, Universitat Politècnica de Catalunya, Carrer Pere Serra 1-15, 08173 Sant Cugat del Vallès, Spain

⁴ School of Earth and Space Exploration, Arizona State University, Tempe, AZ, USA

⁵ Joint Institute for Nuclear Astrophysics Center for the Evolution of the Elements, USA

⁶ Institut d'Astrophysique de Paris, CNRS-Sorbonne Université, 98 bis boulevard Arago, 75014, Paris, France

⁷ Department of Physics and Astronomy & Pittsburgh Particle Physics, Astrophysics, and Cosmology Center (PITT PACC), University of Pittsburgh, 3941 O'Hara Street, Pittsburgh, PA 15260, USA

Received 28 September 2021; accepted 26 January 2022

ABSTRACT

Context. At present, there are strong indications that white dwarf (WD) stars with masses well below the Chandrasekhar limit ($M_{\text{Ch}} \approx 1.4 M_{\odot}$) contribute a significant fraction of SN Ia progenitors. The relative fraction of stable iron-group elements synthesized in the explosion has been suggested as a possible discriminant between M_{Ch} and sub- M_{Ch} events. In particular, it is thought that the higher-density ejecta of M_{Ch} WDs, which favours the synthesis of stable isotopes of nickel, results in prominent [Ni II] lines in late-time spectra ($\gtrsim 150$ d past explosion).

Aims. We study the explosive nucleosynthesis of stable nickel in SNe Ia resulting from M_{Ch} and sub- M_{Ch} progenitors. We explore the potential for lines of [Ni II] in the optical and near-infrared (at 7378 Å and 1.94 μm) in late-time spectra to serve as a diagnostic of the exploding WD mass.

Methods. We reviewed stable Ni yields across a large variety of published SN Ia models. Using 1D M_{Ch} delayed-detonation and sub- M_{Ch} detonation models, we studied the synthesis of stable Ni isotopes (in particular, ^{58}Ni) and investigated the formation of [Ni II] lines using non-local thermodynamic equilibrium radiative-transfer simulations with the CMFGEN code.

Results. We confirm that stable Ni production is generally more efficient in M_{Ch} explosions at solar metallicity (typically 0.02–0.08 M_{\odot} for the ^{58}Ni isotope), but we note that the ^{58}Ni yield in sub- M_{Ch} events systematically exceeds 0.01 M_{\odot} for WDs that are more massive than one solar mass. We find that the radiative proton-capture reaction $^{57}\text{Co}(p, \gamma)^{58}\text{Ni}$ is the dominant production mode for ^{58}Ni in both M_{Ch} and sub- M_{Ch} models, while the α -capture reaction on ^{54}Fe has a negligible impact on the final ^{58}Ni yield. More importantly, we demonstrate that the lack of [Ni II] lines in late-time spectra of sub- M_{Ch} events is not always due to an under-abundance of stable Ni; rather, it results from the higher ionization of Ni in the inner ejecta. Conversely, the strong [Ni II] lines predicted in our 1D M_{Ch} models are completely suppressed when ^{56}Ni is sufficiently mixed with the innermost layers, which are rich in stable iron-group elements.

Conclusions. [Ni II] lines in late-time SN Ia spectra have a complex dependency on the abundance of stable Ni, which limits their use in distinguishing among M_{Ch} and sub- M_{Ch} progenitors. However, we argue that a low-luminosity SN Ia displaying strong [Ni II] lines would most likely result from a Chandrasekhar-mass progenitor.

Key words. supernovae: general – Nuclear reactions, nucleosynthesis, abundances – Radiative transfer – supernovae: individual: SN 2017bzc

1. Introduction

In the long-standing model for Type Ia supernovae (SNe Ia), a carbon-oxygen white dwarf (CO WD) star accretes material from a binary companion until it approaches the Chandrasekhar-mass limit for a relativistic degenerate electron plasma ($M_{\text{Ch}} \approx 1.4 M_{\odot}$). While this model provides a robust ignition mechanism for runaway carbon fusion, it is in tension with the observed SN Ia rate (see e.g. Maoz & Mannucci 2012; Livio & Mazzali 2018; Wang 2018; Soker 2019 for reviews). Moreover, there is growing evidence that it cannot explain the full range of observed SN Ia properties (e.g. Jha et al. 2019). For instance, Flörs et al. (2020) find that the Ni/Fe abundance ratio inferred from

late-time spectroscopy is consistent with the predictions of sub- M_{Ch} models for 85% of normal SNe Ia.

There are multiple paths leading to the explosion of a WD significantly below the Chandrasekhar-mass limit. In double-detonation models (e.g. Shen et al. 2018; Townsley et al. 2019; Magee et al. 2021; Gronow et al. 2021), a sub- M_{Ch} WD accretes a thin He-rich layer from a non-degenerate binary companion, triggering a detonation at its base which leads to a secondary detonation of the CO core. Modern incarnations of this model consider modestly CO-enriched low-mass He layers ($\lesssim 10^{-2} M_{\odot}$), whose detonation does not lead to spurious spectroscopic features from iron-group elements (IGEs) at early times (Shen & Moore 2014; Townsley et al. 2019). Furthermore, the predicted

rate of double-detonation models matches the observed SN Ia rate (e.g. [Ruiter et al. 2011, 2014](#)).

Other sub- M_{Ch} progenitor models involve double-WD systems. In the classical double-degenerate model of [Webbink \(1984\)](#), two unequal-mass WDs in a close binary system merge through loss of energy and angular momentum via gravitational-wave radiation. The more massive WD tidally disrupts and accretes the lower-mass object, resulting in an off-centre carbon ignition in the merger remnant and the formation of an oxygen-neon (ONe) WD (e.g. [Saio & Nomoto 1985](#); [Timmes et al. 1994](#); [Shen et al. 2012](#)). If the remnant mass exceeds the Chandrasekhar limit, accretion-induced collapse to a neutron star ensues, associated with a weak explosion, but with no SN Ia event ([Nomoto & Kondo 1991](#)).

This model was later revised by [Pakmor et al. \(2010\)](#), who considered the merger of two nearly equal-mass WDs, in which the less massive WD is rapidly accreted onto the primary WD, resulting in compressional heating of the accreted material and subsequent carbon ignition. Such violent merger models have been successful in reproducing the observed properties of both sub-luminous and normal SNe Ia ([Pakmor et al. 2010, 2012](#)), as well as more peculiar events ([Kromer et al. 2013, 2016](#)).

In addition to mergers, several authors have explored collisions between two WDs as a potential SN Ia progenitor scenario (e.g. [Raskin et al. 2009](#); [Rosswog et al. 2009](#)). Such collisions are expected to occur in dense stellar environments such as globular clusters (e.g. [Hut & Inagaki 1985](#); [Sigurdsson & Phinney 1993](#)); it was more recently suggested that they may efficiently occur in triple systems to explain SNe Ia ([Katz & Dong 2012](#); [Kushnir et al. 2013](#)), although the predicted rates vary significantly (see e.g. [Toonen et al. 2018](#)). Furthermore, [Dong et al. \(2015\)](#) argued that the doubly peaked line profiles observed in late-time spectra of several SNe Ia result from a bimodal ^{56}Ni distribution produced in WD-WD collisions.

It should be possible to identify SNe Ia resulting from M_{Ch} vs. sub- M_{Ch} progenitors observationally, since variations in the ejecta mass have an impact on the radiative display (e.g. [Pinto & Eastman 2000](#)). The typical photon diffusion time depends on the mean opacity, κ , of the ejecta, its mass, M_{ej} , and characteristic velocity, v , following $t_{\text{diff}} \propto \kappa^{1/2} M_{\text{ej}}^{1/2} v^{-1/2}$ (e.g. [Arnett 1982](#); [Woosley et al. 2007](#); [Piro et al. 2010](#); [Khatami & Kasen 2019](#)). The photon diffusion time is thus shorter for a sub- M_{Ch} ejecta compared to a M_{Ch} ejecta, resulting in shorter bolometric rise times (see e.g. [Blondin et al. 2017](#)). The post-maximum bolometric decline is also faster, as the lower density of sub- M_{Ch} ejecta favours the earlier escape of γ -rays (e.g. [Kushnir et al. 2020](#); [Sharon & Kushnir 2020](#))¹.

The colour evolution around maximum light is also affected by the ejecta mass. As noted by [Blondin et al. \(2017\)](#), sub- M_{Ch} ejecta are subject to a larger specific heating rate at maximum light² for a given ^{56}Ni mass, owing to the shorter rise times and lower ejecta mass; hence, they display bluer maximum-light colours. The colour evolution past maximum light is also more pronounced, as observed in low-luminosity SNe Ia (e.g. [Blondin et al. 2017](#); [Shen et al. 2021](#)). The ejecta mass can, in principle, be constrained based purely on photometric indicators. In practice, however, their interpretation is subject to uncertainties in

the radiative-transfer modelling (see e.g. discussion in [Blondin et al. 2018](#)).

A more robust signature of the WD mass should therefore be sought in the spectroscopic signatures of distinct abundance patterns predicted by different explosion models; in particular, the density at which the CO fuel is ignited affects the resulting nucleosynthesis. More specifically, Chandrasekhar-mass WDs have central densities $\rho_c \gtrsim 10^9 \text{ g cm}^{-3}$, where explosion models involving sub- M_{Ch} WDs (including WD mergers and collisions) detonate the CO core in regions with $\rho \lesssim 10^8 \text{ g cm}^{-3}$. The higher densities in M_{Ch} models result in a higher electron-capture rate during the explosion, which enhances the production of neutron-rich stable isotopes of iron-group elements compared to sub- M_{Ch} models.

Of particular interest are the stable isotopes of nickel, the most abundant of which is ^{58}Ni . At sufficiently late times ($\gtrsim 150 \text{ d}$ past explosion), SN Ia spectra are dominated by forbidden lines of singly and doubly ionized Ni, Co, and Fe. By then, the only nickel left in the ejecta is stable Ni synthesized in the explosion, whereas most of the Co is ^{56}Co from ^{56}Ni decay, and Fe is a mixture of primordial stable Fe and ^{56}Fe from ^{56}Ni decay. The larger abundance of stable Ni in M_{Ch} models is thus expected to manifest itself in the form of forbidden lines of [Ni II], which have been detected in late-time spectra of several SNe Ia to date (e.g. [Dhawan et al. 2018](#); [Maguire et al. 2018](#); [Flörs et al. 2018, 2020](#)). These lines ought to be largely suppressed if not completely absent from sub- M_{Ch} models due to the lower abundance of stable Ni.

In principle, we thus have a clear prediction in terms of stable Ni production that depends on the mass of the exploding WD and an associated spectroscopic diagnostic to distinguish between M_{Ch} and sub- M_{Ch} models. This was partly confirmed by [Blondin et al. \(2018\)](#) for low-luminosity SN Ia models: the M_{Ch} model displayed a prominent line due to [Ni II] $1.94 \mu\text{m}$, where the sub- M_{Ch} model showed no such line.

In this paper, we test whether this prediction holds for higher-luminosity models, which correspond to the bulk of the SN Ia population, and to what extent the abundance of stable Ni is the determining factor in explaining the strength of [Ni II] lines in late-time SN Ia spectra. We first briefly present the SN Ia models and numerical methods in Sect. 2. We investigate the dominant nuclear reactions responsible for stable Ni production and present a census of ^{58}Ni yields in M_{Ch} versus sub- M_{Ch} models in Sect. 3. We discuss the relative impact of Ni abundance and ionization on nebular [Ni II] lines in Sect. 4, as well as the impact of mixing in Sect. 5. Our conclusions follow in Sect. 6.

2. Explosion models and radiative transfer

We base our analysis on previously published SN Ia explosion models. One exception is the 1D M_{Ch} delayed-detonation model 5p0_Z0p014, published here for the first time, whose WD progenitor results from the evolution of a $5 M_{\odot}$ star at solar metallicity ($Z = 0.014$; [Asplund et al. 2009](#)). The explosive phase was simulated using the same hydrodynamics and nucleosynthesis code as the sub- M_{Ch} detonation models 1p06_Z2p25e-2 and 0p88_Z2p25e-2 from a $1.06 M_{\odot}$ and $0.88 M_{\odot}$ WD progenitor, respectively, at slightly super-solar metallicity ($Z = 0.025 \approx 1.6 Z_{\odot}$; [Bravo et al. 2019](#)). Basic model properties and various nickel isotopic abundances are given in Table A.1.

The synthetic late-time spectra ($\sim 190 \text{ d}$ past explosion) presented in Sects. 4 and 5 were computed using the 1D, time-dependent, non-local thermodynamic equilibrium radiative-transfer code CMFGEN of [Hillier & Dessart \(2012\)](#). Late-

¹ We note, however, that both of these studies argue that observed SN Ia light curves are in tension with the γ -ray escape time scales inferred for sub- M_{Ch} models.

² defined as $\dot{e}_{\text{decay}}(t_{\text{max}}) = L_{\text{decay}}(t_{\text{max}})/M_{\text{tot}}$, where $L_{\text{decay}}(t_{\text{max}})$ is the decay luminosity at maximum light and M_{tot} is the ejecta mass.

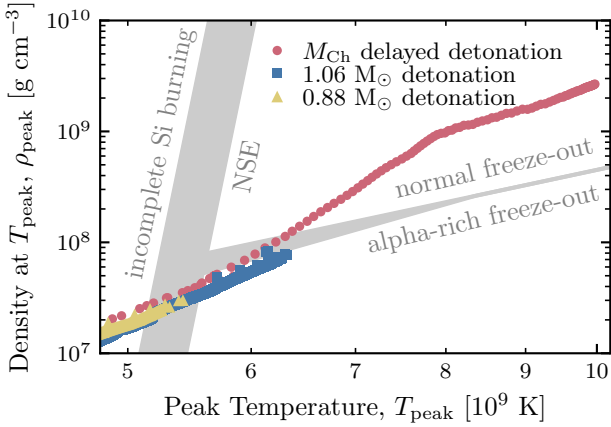


Fig. 1. Density at peak temperature (ρ_{peak}) versus peak temperature (T_{peak} , in units of 10^9 K) in the M_{Ch} delayed-detonation model 5p0_Z0p014 (filled circles) and the sub- M_{Ch} detonation models 1p06_Z2p25e-2 ($M_{\text{WD}} = 1.06 M_{\odot}$, filled squares) and 0p88_Z2p25e-2 ($M_{\text{WD}} = 0.88 M_{\odot}$, filled triangles). The wide vertical band denotes the transition between incomplete Si burning and complete burning to NSE. The NSE region is further subdivided into ‘normal’ and ‘alpha-rich’ freeze-out regimes. The width of the bands correspond to variations in the post-burn cooling time scale (Woosley et al. 1973; see also Lach et al. 2020, their Fig. 1).

time spectra for the low-luminosity M_{Ch} delayed-detonation model DDC25 and the sub- M_{Ch} detonation model SCH2p0 are from Blondin et al. (2018). Those for the high-luminosity M_{Ch} delayed-detonation model DDC0 and the sub- M_{Ch} detonation model SCH7p0 are published here for the first time. The same is true of the mixed versions of the M_{Ch} delayed-detonation model DDC15 (Sect. 5). All model outputs are publicly available on-line³.

3. Stable Ni production in M_{Ch} vs. sub- M_{Ch} models

3.1. Nuclear statistical equilibrium

Explosive burning at sufficiently high temperatures ($T \gtrsim 5 \times 10^9$ K) results in a state of balance between forward and reverse nuclear reactions known as nuclear statistical equilibrium (NSE; see e.g. Clifford & Tayler 1965; Woosley et al. 1973; Hartmann et al. 1985; Cabezón et al. 2004; Nadyozhin & Yudin 2004). Such temperatures are reached in the inner layers of both M_{Ch} delayed-detonation models and sub- M_{Ch} detonation models, although the highest temperatures $\lesssim 10^{10}$ K are only reached in M_{Ch} models (Fig. 1). In NSE, the yields do not depend on the initial composition but are instead uniquely determined by the peak temperature (T_{peak}), the density at T_{peak} (ρ_{peak}), and the electron fraction, $Y_e = \sum_i (Z_i/A_i)X_i$, where X_i is the mass fraction of a particular isotope i with atomic number Z_i and mass number A_i .

The electron fraction of the WD prior to explosion is set by the metallicity of the progenitor star on the main sequence, which is routinely parametrized by adjusting the abundance of the neutron-rich isotope ^{22}Ne . Here, the assumption is that the CNO catalysts all end up as ^{14}N at the end of the hydrogen-burning phase, which is then converted to ^{22}Ne via

$^{14}\text{N}(\alpha, \gamma)^{18}\text{F}(\beta^+, \nu_e)^{18}\text{O}(\alpha, \gamma)^{22}\text{Ne}$ during the helium-core burning phase (see Timmes et al. 2003), such that:

$$X(^{22}\text{Ne}) = 22 \left[\frac{X(^{12}\text{C})}{12} + \frac{X(^{14}\text{N})}{14} + \frac{X(^{16}\text{O})}{16} \right] \approx 0.013 \left(\frac{Z}{Z_{\odot}} \right), \quad (1)$$

where we used the solar CNO abundances from Asplund et al. (2009) and isotopic ratios from Lodders (2003)⁴. We ignore the initial ^{22}Ne of the progenitor star as its mass fraction is $\sim 10^{-4}$ at solar metallicity.

In addition to ^{22}Ne resulting from the CNO cycle, the initial metallicity is also determined by the abundance of ^{56}Fe nuclei inherited from the ambient interstellar medium. For a WD composed of only ^{12}C , ^{16}O , ^{22}Ne , and ^{56}Fe (i.e. $X(^{12}\text{C}) + X(^{16}\text{O}) = 1 - X(^{22}\text{Ne}) - X(^{56}\text{Fe})$), the electron fraction is (see also Kushnir et al. 2020):

$$\begin{aligned} Y_e &= \frac{6}{12}X(^{12}\text{C}) + \frac{8}{16}X(^{16}\text{O}) + \frac{10}{22}X(^{22}\text{Ne}) + \frac{26}{56}X(^{56}\text{Fe}) \\ &= \frac{1}{2} - \frac{X(^{22}\text{Ne})}{22} - \frac{X(^{56}\text{Fe})}{28} \\ &\approx \frac{1}{2} - 6.5 \times 10^{-4} \left(\frac{Z}{Z_{\odot}} \right), \end{aligned} \quad (2)$$

where we have used the solar Fe abundance $X(\text{Fe}) = 1.292 \times 10^{-3}$ from Asplund et al. (2009) and the ^{56}Fe isotopic fraction of 91.754% from Lodders (2003), yielding $X(^{56}\text{Fe}) \approx 1.185 \times 10^{-3}(Z/Z_{\odot})$. In this framework, a solar-metallicity WD has $X(^{22}\text{Ne}) \approx 0.013^5$ and $Y_e \approx 0.49935$. A larger metallicity corresponds to a larger ^{22}Ne abundance and in turn a lower Y_e .

In M_{Ch} models this baseline Y_e can, in principle, be reduced via weak reactions on carbon during the convective burning (or ‘simmering’) phase prior to thermonuclear runaway (e.g. Piro & Bildsten 2008; Chamulak et al. 2008; Schwab et al. 2017), although Martínez-Rodríguez et al. (2016) show the impact to be negligible (reduction in Y_e of $\lesssim 10^{-4}$; but see Piersanti et al. 2017 for a different view). However, the higher densities of M_{Ch} WDs (up to $2\text{--}3 \times 10^9$ g cm $^{-3}$; see Fig. 1) result in a significant electron-capture rate during the initial deflagration phase of delayed-detonation models. This lowers the Y_e far below the baseline value (Fig. 2, top panel) and favours the synthesis of neutron-rich isotopes in the innermost layers ($v \lesssim 3000$ km s $^{-1}$; Fig. 2, middle panel). For nickel, this results in the synthesis of the stable isotopes ^{58}Ni , ^{60}Ni , ^{61}Ni , ^{62}Ni , and ^{64}Ni instead of the radioactive ^{56}Ni (for which $Y_e = 0.5$).

In detonations of sub- M_{Ch} WDs, however, the burning timescale is much shorter than the weak-reaction timescale, such that Y_e remains constant at its baseline value ($Y_e \approx 0.49935$ for a solar-metallicity WD) throughout the burning phase. Stable neutron-rich isotopes of nickel are still synthesized in NSE at this Y_e at the peak temperatures ($5\text{--}6 \times 10^9$ K) and densities ($10^7\text{--}10^8$ g cm $^{-3}$), characteristic of the inner ejecta of sub- M_{Ch}

⁴ Kushnir et al. (2020) adopt the slightly higher value of $X(^{22}\text{Ne}) \approx 0.015(Z/Z_{\odot})$ to account for the expected higher solar bulk abundances compared to the photospheric values (see e.g. Turcotte & Wimmer-Schweingruber 2002).

⁵ Kobayashi et al. (2020) adopt a different approach in their solar-scaled initial composition models by assuming that all the ^{22}Ne is inherited from the progenitor with no contribution from CNO. This results in a much lower ^{22}Ne mass fraction at a given metallicity (although we were not able to confirm the exact value), which has a significant impact on the stable Ni yields in their models (see Sect. 3.5).

³ <https://zenodo.org/record/5528088>

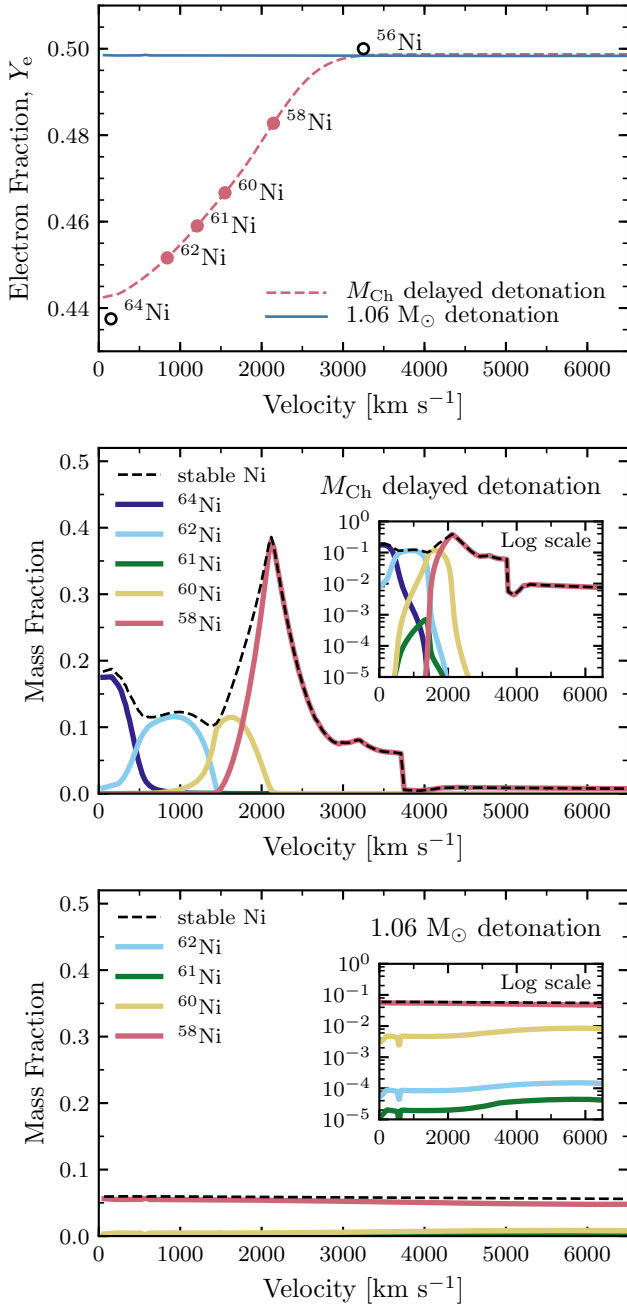


Fig. 2. Top panel: Electron fraction profile at $t \approx 30$ min past explosion in the inner ejecta of the M_{Ch} delayed-detonation model 5p0_Z0p014 (dashed line) and the $M_{\text{WD}} = 1.06 M_{\odot}$ sub- M_{Ch} detonation model 1p06_Z2p25e-2 (solid line) shown in Fig. 1. The markers in the upper panel are shown such that the ordinate corresponds to the Y_e of the nucleus (e.g. $Y_e = 28/58 \approx 0.483$ for ^{58}Ni) and the abscissa to the interpolated velocity on the Y_e profile for the M_{Ch} delayed-detonation model (both ^{56}Ni and ^{64}Ni are synthesized in this model but the Y_e profile does not intersect the Y_e value of either isotope). Middle and bottom panels: Abundance profiles of stable Ni isotopes for both models. The insets correspond to a logarithmic scale, revealing minor contributions to the total stable Ni abundance from ^{61}Ni for the M_{Ch} model and from both ^{61}Ni and ^{62}Ni for the sub- M_{Ch} model. No ^{64}Ni is produced in this sub- M_{Ch} model.

detonations (Fig. 2, bottom panel). These conditions are similar to those encountered in the layers of M_{Ch} models where most of the ^{58}Ni is synthesized ($v \approx 2000$ km s⁻¹ for the M_{Ch} model shown in Fig. 2). By comparing the NSE distributions for

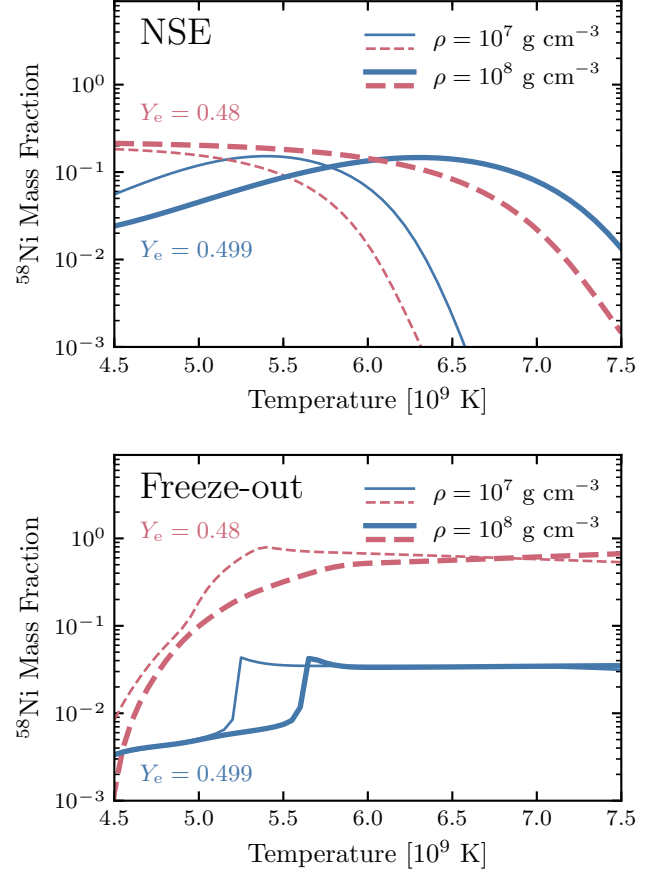


Fig. 3. Top panel: NSE distributions for ^{58}Ni as a function of temperature (in units of 10⁹ K) for $Y_e = 0.48$ (dashed lines) and $Y_e = 0.499$ (solid lines), at densities of 10^7 g cm⁻³ (thin lines) and 10^8 g cm⁻³ (thick lines). These NSE distributions were computed with the public_nse code ⁶ (see also Seitenzahl et al. 2008). Bottom panel: Freeze-out yields based on the adiabatic thermodynamic trajectories of Magkotsios et al. (2010) for the same set of $(\rho_{\text{peak}}, Y_e)$ values.

$Y_e = 0.499$ and $Y_e = 0.48$ in Fig. 3 (top panel), we see that the ^{58}Ni abundance in sub- M_{Ch} detonations can be comparable to (and even exceed) that of M_{Ch} delayed-detonation models, with predicted mass fractions $X(^{58}\text{Ni}) \approx 0.1$.

3.2. Freeze-out yields

The final isotopic abundances can differ significantly from their NSE value during the so-called freeze-out phase, when free particles (protons, neutrons, α particles) reassemble into nuclei on a timescale of $\propto 1/\sqrt{\rho}$ (e.g. Magkotsios et al. 2010). For high densities ($\gtrsim 10^8$ – 10^9 g cm⁻³), this timescale is short and for $T \lesssim 7 \times 10^9$ K the α abundance is low (normal freeze-out), such that the final abundances do not differ greatly from their NSE value. However, for the lower ρ_{peak} relevant to the synthesis of ^{58}Ni (10^7 – 10^8 g cm⁻³), the freeze-out timescale is longer and the α abundance is higher ($X(^4\text{He}) \approx 0.1$; alpha-rich freeze-out), and the final yields of stable Ni isotopes can differ significantly from their NSE values (Fig. 3, bottom panel).

In either case, the freeze-out timescale is significantly shorter than the weak-reaction timescale, such that Y_e remains roughly constant during the freeze-out. Stable isotopes of Ni are syn-

⁶ Publicly available on F. X. Timmes' webpage; http://cococubed.asu.edu/code_pages/nse.shtml

thesized preferentially in shells with a similar Y_e value. This is illustrated by the M_{Ch} delayed-detonation model in the bottom panel of Fig. 2, where the peak in the stable Ni abundance profile at $\sim 2000 \text{ km s}^{-1}$ consists almost exclusively of the ^{58}Ni isotope (see inset). The Y_e of this isotope ($Y_e = 28/58 \approx 0.48$) coincides with the Y_e value at this velocity coordinate (Fig. 2, top panel), where the peak temperature is $\sim 5 \times 10^9 \text{ K}$ and the density $2\text{--}3 \times 10^7 \text{ g cm}^{-3}$. Under these conditions, the predicted freeze-out mass fraction for ^{58}Ni is a few times 0.1 (Fig. 3, bottom panel), which is on par with the M_{Ch} model yield. The more neutron-rich isotopes ^{60}Ni , ^{61}Ni , ^{62}Ni , and ^{64}Ni are synthesized at lower velocities $\lesssim 1500 \text{ km s}^{-1}$, where the density is higher – and hence the Y_e value is lower as a result of electron captures.

For the sub- M_{Ch} detonation model, the stable Ni mass fraction remain roughly constant at $5\text{--}6 \times 10^{-2}$ throughout the inner ejecta. These mass fractions are in agreement with the predicted freeze-out ^{58}Ni yields for $Y_e = 0.499$ and densities in the range $10^7\text{--}10^8 \text{ g cm}^{-3}$ for peak temperatures $5\text{--}6 \times 10^9 \text{ K}$ (Fig. 3, bottom panel). In M_{Ch} models, ^{58}Ni is synthesized in layers with similar ($T_{\text{peak}}, \rho_{\text{peak}}$) conditions, but at a lower $Y_e \approx 0.48$, which results in an order-of-magnitude difference in the predicted freeze-out yields.

3.3. Decayed yields at one year past explosion

Once the burning phase has ceased (typically a few seconds after the beginning of the thermonuclear runaway), the stable Ni yield continues to increase through radioactive decays with half-lives $t_{1/2} \gtrsim 1 \text{ s}$, in particular via the β^+ decay chains $^{60,61,62}\text{Zn} \rightarrow ^{60,61,62}\text{Cu} \rightarrow ^{60,61,62}\text{Ni}$ (see Table 1). From this point, we go on to consider the decayed yields at one year past explosion when referring to the ^{58}Ni or stable Ni yields, as these are most relevant to the late-time spectra discussed in this paper. We note, however, that the decayed ^{58}Ni yield is set shortly after explosion, since the only parent isotope, ^{58}Cu , decays to ^{58}Ni with a half-life of $\sim 3.2 \text{ s}$.

3.4. Synthesis of the stable isotope ^{58}Ni

For all the models studied here with a ^{58}Ni yield larger than $0.01 M_{\odot}$, more than 60% of all the stable Ni is in the form of ^{58}Ni (see Table A.1)⁷. This fraction rises above 80% for models with a ^{58}Ni yield larger than $0.04 M_{\odot}$. For comparison, the isotopic fraction of ^{58}Ni on Earth and in the Sun is $\sim 68\%$ (Lodders 2003). In both the M_{Ch} delayed-detonation model 5p0_Z0p014 and the sub- M_{Ch} detonation model 1p06_Z2p25e-2 (described in the previous section), this isotope is mainly synthesized through the reactions depicted in Fig. 4, where the reaction probabilities correspond to the aforementioned sub- M_{Ch} model. They were obtained by integrating the net reaction fluxes (mol g^{-1}) and calculating the relative contributions of each reaction to the total net flux. Thus, in this model, ^{57}Cu is synthesized 81.5% of the time via $^{56}\text{Ni}(p, \gamma)$ and the remaining 18.5% via $^{60}\text{Zn}(p, \alpha)$. The probabilities do not always add up to 100%, as other more minor reactions can contribute to a specific isotope. Most notably ^{58}Ni is also synthesized via $^{58}\text{Co}(p, n)$ (6.13%), $^{61}\text{Cu}(p, \alpha)$ (4.85%), $^{55}\text{Fe}(\alpha, n)$ (2.26%), $^{54}\text{Fe}(\alpha, \gamma)$ (2.04%), $^{57}\text{Ni}(n, \gamma)$ (1.25%), $^{58}\text{Cu}(n, p)$ (0.51%), $^{62}\text{Zn}(\gamma, \alpha)$ (0.38%), and

Table 1. Radioactive decay chains with half-lives $t_{1/2} > 1 \text{ s}$ ending in a stable isotope of nickel.

Parent Isotope	Daughter Isotope	Half-life $t_{1/2}$	Decay Mode [Branching %]	Final Product
^{58}Cu	^{58}Ni	3.204(7) s	$\epsilon + \beta^+$	^{58}Ni
^{60}Mn	^{60}Fe	51(6) s	β^-	^{60}Ni
^{60}Fe	^{60}Co	$2.62(4) \times 10^6 \text{ y}$	β^-	^{60}Ni
^{60}Co	^{60}Ni	5.2714(6) y	β^-	^{60}Ni
^{60}Zn	^{60}Cu	2.38(5) m	$\epsilon + \beta^+$	^{60}Ni
^{61}Fe	^{61}Co	5.98(6) m	β^-	^{61}Ni
^{61}Co	^{61}Ni	1.650(5) h	β^-	^{61}Ni
^{61}Zn	^{61}Cu	89.1(2) s	$\epsilon + \beta^+$	^{61}Ni
^{61}Cu	^{61}Ni	3.333(5) h	$\epsilon + \beta^+$	^{61}Ni
^{62}Fe	^{62}Co	68(2) s	β^-	^{62}Ni
^{62}Co	^{62}Ni	1.50(4) m	β^-	^{62}Ni
^{62}Zn	^{62}Cu	9.186(13) h	$\epsilon + \beta^+$	^{62}Ni
^{62}Cu	^{62}Ni	9.74(2) m	$\epsilon + \beta^+$	^{62}Ni
^{64}Fe	^{64}Co	2.0(2) s	β^-	^{64}Ni
^{64}Co	^{64}Ni	0.30(3) s	β^-	^{64}Ni
^{64}Cu	^{64}Ni	12.700(2) h	$\epsilon + \beta^+ [61.0(3)]$	^{64}Ni

Notes: Data are from Chu et al. (1999) except for the half-life for $^{60}\text{Fe} \rightarrow ^{60}\text{Co}$, which is taken from Rugel et al. (2009). Numbers in parentheses are the 1σ uncertainty on the last digit. Numbers in square brackets give the branching ratio (%), which is implicitly 100% when not given. The decay mode ϵ refers to electron capture (EC). Although its half-life is less than 1 s, we report the $^{64}\text{Co} \rightarrow ^{64}\text{Ni}$ decay since it is part of the $^{64}\text{Fe} \rightarrow ^{64}\text{Co} \rightarrow ^{64}\text{Ni}$ decay chain. We do not consider excited nuclear isomer states of $^{60\text{m}}\text{Mn}$, $^{60\text{m}}\text{Co}$, or $^{62\text{m}}\text{Co}$.

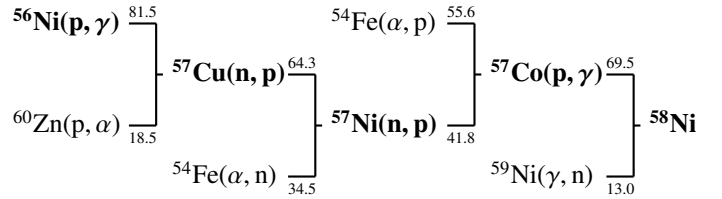


Fig. 4. Main reactions resulting in the synthesis of stable ^{58}Ni . The numbers give the probability for a given reaction product to result from a specific reactant in the sub- M_{Ch} model 1p06_Z2p25e-2 (see text for details).

$^{61}\text{Zn}(n, \alpha)$ (0.01%), in addition to the two dominant reactions $^{57}\text{Co}(p, \gamma)$ (69.5%) and $^{59}\text{Ni}(\gamma, n)$ (13.0%).

The dominant reaction chain is highlighted in bold: $^{56}\text{Ni}(p, \gamma)^{57}\text{Cu}(n, p)^{57}\text{Ni}(n, p)^{58}\text{Ni}$. The probability for a ^{58}Ni nucleus to result from a particular reactant nucleus is simply obtained by multiplying the reaction probabilities along the chain. Thus $0.815 \times 0.643 \times 0.418 \times 0.695 \approx 0.152$ or 15.2% of ^{58}Ni nuclei result from the reaction chain starting with ^{56}Ni in this model. The majority of ^{56}Ni does not end up as ^{58}Ni , of course, as many ^{56}Ni nuclei survive the explosive phase to later decay radioactively via the $^{56}\text{Ni} \rightarrow ^{56}\text{Co} \rightarrow ^{56}\text{Fe}$ chain and power the SN Ia light curve.

Among all reactions ending in ^{58}Ni , the final ^{58}Ni abundance is mostly determined by the rate for the radiative proton-capture reaction $^{57}\text{Co}(p, \gamma)^{58}\text{Ni}$. This might appear surprising since an α -rich freeze-out from NSE should favour α captures on ^{54}Fe as the main production route for ^{58}Ni , in particular $^{54}\text{Fe}(\alpha, \gamma)^{58}\text{Ni}$. However, this reaction only contributes $\sim 2\%$ of the net nucleosynthetic flux to ^{58}Ni in this model. In spite of the seemingly large contribution of $^{54}\text{Fe}(\alpha, p)$ to the synthesis of ^{57}Co (34.5%) and of $^{54}\text{Fe}(\alpha, n)$ to that of ^{57}Ni (55.6%), artificially inhibiting

⁷ The only exception is the double-detonation model of Townsley et al. (2019), with a ^{58}Ni isotopic fraction of $\sim 44.7\%$. A large fraction of the stable nickel in this model is in the form of ^{60}Ni (44.9%) which results from the radioactive decay of ^{60}Zn .

all α captures (with either γ , neutron or proton output channels) on ^{54}Fe has a negligible impact on the final ^{58}Ni abundance compared to when the radiative proton-capture reaction $^{57}\text{Co}(p, \gamma)^{58}\text{Ni}$ is artificially switched off.

Nonetheless, the preferred reaction chain from ^{54}Fe to ^{58}Ni during freeze-out mimics the α -capture reaction $^{54}\text{Fe}(\alpha, \gamma)^{58}\text{Ni}$, as it proceeds first via two radiative proton captures to ^{56}Ni , namely, $^{54}\text{Fe}(p, \gamma)^{55}\text{Co}(p, \gamma)^{56}\text{Ni}$, followed by the reaction chain outlined in bold above from ^{56}Ni to ^{58}Ni . The entire process then consists of four (p, γ) and two (n, p) reactions, which is indeed equivalent to the net capture of an α particle ($2n + 2p$). While the abundance of α particles is large in α -rich freeze-out by definition, the abundance of free neutrons and protons is even more enhanced compared to that in a normal freeze-out.

Although the $^{57}\text{Co}(p, \gamma)^{58}\text{Ni}$ reaction dominates the reaction chain ending in ^{58}Ni , the synthesis of this isotope in Chandrasekhar-mass WDs is mostly affected by the amount of electron captures in NSE. Since ^{56}Ni is the most abundant isotope when NSE is achieved at the neutron excess inherited from the progenitor (see Fig. 2), the yield of ^{58}Ni is most sensitive to the electron-capture rate on ^{56}Ni and, to a lesser extent, on ^{55}Co . However, the yield of ^{58}Ni is quite robust as it changes by $\sim 20\%$ for a two orders-of-magnitude change in any electron-capture rate (see Bravo 2019 for more details).

3.5. ^{58}Ni yields in M_{Ch} and sub- M_{Ch} models

We show the decayed ^{58}Ni yield at $t = 1$ yr past explosion as a function of the ^{56}Ni mass at $t \approx 0$ for a variety of SN Ia explosion models in Fig. 5. In the following subsections, we first discuss M_{Ch} models and then sub- M_{Ch} models. We include violent WD mergers and WD collisions in sub- M_{Ch} models since the mass of the exploding WD is below M_{Ch} , despite the combined mass of both WDs sometimes exceeding this value.

3.5.1. Chandrasekhar-mass models

Deflagrations: Laminar flames in SNe Ia quickly become turbulent as buoyant hot ashes rise through overlying cold fuel, generating Rayleigh-Taylor and Kelvin-Helmholtz instabilities that increase the flame surface and hence the rate of fuel consumption. Deflagrations are thus best studied in 3D, and we base our discussion on the models of Fink et al. (2014)⁸. Since the precise initial conditions at the onset of thermonuclear runaway remain unknown to a large extent, the deflagration is artificially ignited in a number N_k of spherical ignition spots (or ‘kernels’) simultaneously. In their study, Fink et al. (2014) consider $N_k = 1, 3, 5, 10, 20, 40, 100, 150, 200, 300$, and 1600 such kernels distributed at random around the WD centre.

As N_k increases, the rate of fuel consumption (and hence nuclear energy release) also increases, resulting in a more rapid flame growth and more material being burnt. Thus, increasing N_k results in a higher production of both stable ^{58}Ni and radioactive ^{56}Ni , which explains the monotonic sequence in Fig. 5 (open squares) up until $N_k = 150$. For higher N_k , the nuclear energy release is so high early on that the resulting WD expansion quenches nuclear reactions, resulting in less material being burnt. Thus, while the ^{58}Ni yield continues to increase with N_k (as this stable isotope is mainly produced during the initial stages of the deflagration), the ^{56}Ni yield remains more or less constant, even decreasing slightly for $N_k = 1600$ (model N1600def).

⁸ For models that fail to completely unbind the WD, the reported yields also include the ^{58}Ni and ^{56}Ni synthesized in the remnant core.

The models of Fink et al. (2014) enable us to study the impact of variations in the central density of the progenitor WD for model N100def (dashed line in Fig. 5). A lower central density of $\rho_c = 1.0 \times 10^9 \text{ g cm}^{-3}$ results in a $\sim 50\%$ lower ^{58}Ni yield owing to the lower electron-capture rate during the initial deflagration. However, increasing ρ_c to $5.5 \times 10^9 \text{ g cm}^{-3}$ results in a similar ^{58}Ni yield as in the base model with $\rho_c = 2.9 \times 10^9 \text{ g cm}^{-3}$, but the yield of heavier stable Ni isotopes more than doubles (see Table A.1).

For completeness we show the widely used 1D deflagration model W7 of Nomoto et al. (1984) as computed by Mori et al. (2018) with updated electron-capture rates. In this model, the deflagration front is artificially accelerated from 8 to 30% of the local sound speed. The initial propagation of the deflagration flame results in a similar electron-capture rate compared to the most energetic 3D deflagration models of Fink et al. (2014), with a ^{58}Ni yield of $\sim 0.07 M_{\odot}$. However the gradual acceleration of the flame results in a more complete burn of the outer layers and a larger ^{56}Ni yield compared to standard deflagration models. Leung & Nomoto (2018) find similar ^{56}Ni and stable Ni yields but they also consider W7 models at sub-solar metallicities (0.1 and $0.5 Z_{\odot}$). Interestingly, the impact on the stable Ni yield is negligible ($\lesssim 4\%$; see Table A.1).

Delayed detonations: In the 1D delayed-detonation models shown here (DDC series of Blondin et al. 2013), the ^{58}Ni yield is relatively constant at $\sim 0.025 M_{\odot}$ regardless of the ^{56}Ni mass. Stable Ni isotopes are almost exclusively synthesized in high-density burning conditions during the early deflagration phase, with almost no stable Ni produced during the subsequent detonation phase (where most of the radioactive ^{56}Ni is synthesized). The exception is model DDC0 which has the largest ^{56}Ni yield ($0.84 M_{\odot}$) for which an additional $\sim 0.01 M_{\odot}$ of ^{58}Ni is synthesized during the detonation phase at expansion velocities $5000\text{--}8500 \text{ km s}^{-1}$ (corresponding to mass coordinates $\sim 0.3\text{--}0.65 M_{\odot}$), where the peak temperatures reach $5.5\text{--}6.9 \times 10^9 \text{ K}$ at densities $2.5\text{--}5.8 \times 10^7 \text{ g cm}^{-3}$.

The situation is somewhat different in 3D simulations where a substantial amount of stable Ni is synthesized during the detonation phase. The weaker the initial deflagration (i.e. the lower the number of ignition kernels), the smaller the WD pre-expansion prior to the deflagration-to-detonation transition and the higher the burning density during the detonation phase. As a result, more stable IGEs (as well as radioactive ^{56}Ni) are synthesized during the detonation. An extreme example is model N1 (only one ignition kernel ignites the initial deflagration), which synthesizes more than $0.07 M_{\odot}$ of ^{58}Ni and more than $1.1 M_{\odot}$ of ^{56}Ni , but whose deflagration counterpart (N1def) synthesizes less than $0.01 M_{\odot}$ of ^{58}Ni and less than $0.1 M_{\odot}$ of ^{56}Ni . Conversely, one can deduce from comparing models N1600 and N1600def that almost all the stable ^{58}Ni and radioactive ^{56}Ni are synthesized during the deflagration phase, owing to the high number of ignition kernels.

Also shown in Fig. 5 is the impact of varying the central density of the progenitor WD for model N100 (dashed line; see also the 2D models of Kobayashi et al. 2020). As for the deflagration model N100def, a lower central density of $\rho_c = 1.0 \times 10^9 \text{ g cm}^{-3}$ results in a lower ^{58}Ni yield owing to the lower electron-capture rate during the initial deflagration. However, whereas increasing ρ_c had a negligible impact on the production of stable ^{58}Ni for the deflagration model N100def, the ^{58}Ni yield increases by $\sim 9\%$ in the delayed-detonation model N100 owing to pockets of high-density fuel burnt during the subsequent detonation phase.

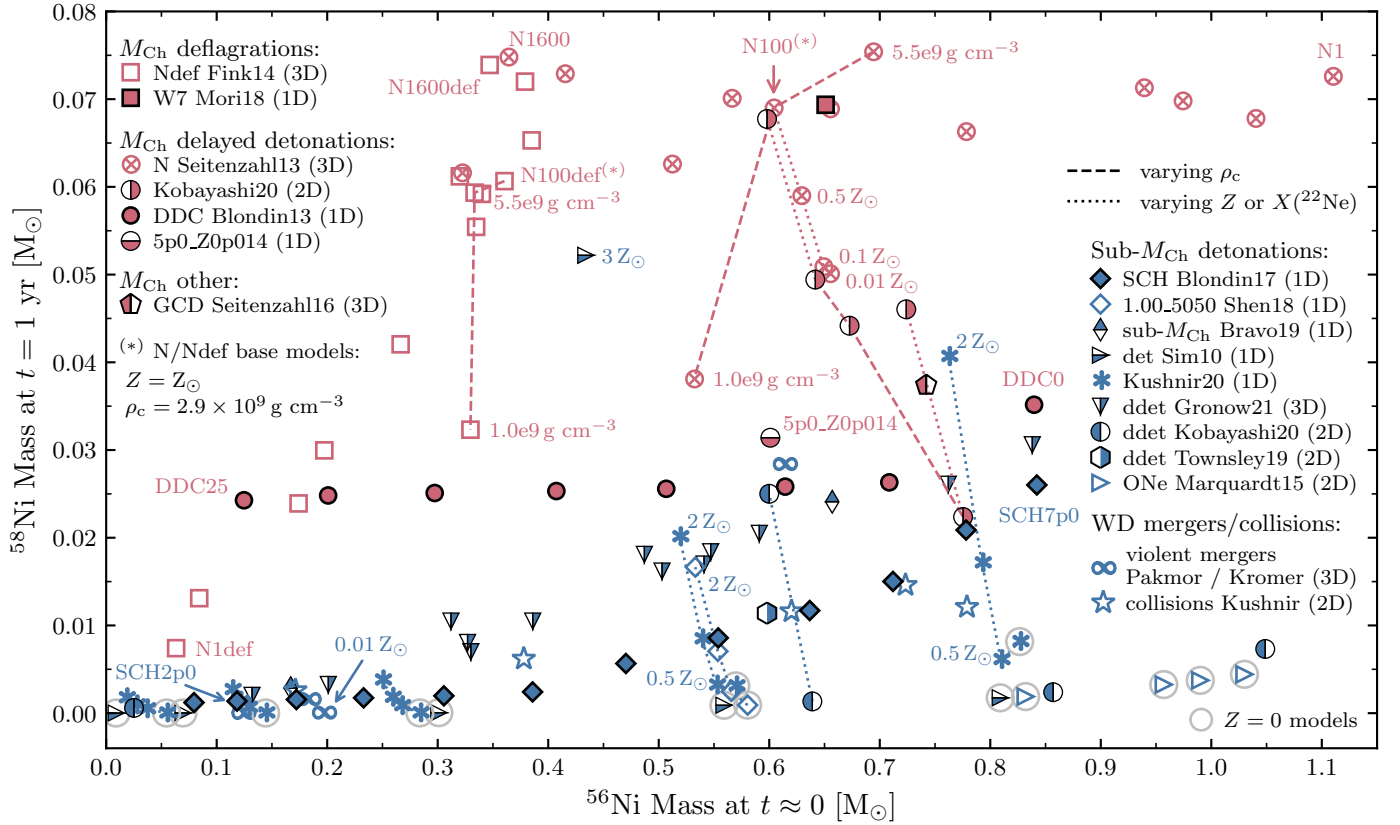


Fig. 5. Stable ^{58}Ni yield at $t = 1$ yr past explosion versus radioactive ^{56}Ni yield at $t \approx 0$ for various SN Ia explosion models (M_{Ch} models in red, sub- M_{Ch} models in blue). Chandrasekhar-mass models include: deflagrations (3D models of Fink et al. 2014; 1D W7 model of Mori et al. 2018), delayed detonations (3D models of Seitenzahl et al. 2013; 2D models of Kobayashi et al. 2020; 1D models of Blondin et al. 2013; 1D model 5p0_Z0p014 from this paper), and gravitationally confined detonations (3D model of Seitenzahl et al. 2016). Sub- M_{Ch} models include: detonations (1D models of Blondin et al. 2017; 1D $1 M_{\odot}$ models of Shen et al. 2018; 1D models of Bravo et al. 2019; 1D models of Sim et al. 2010; 1D models of Kushnir et al. 2020), double detonations (3D models of Gronow et al. 2021; 2D models of Kobayashi et al. 2020; 2D model of Townsley et al. 2019), detonations in ONe WDs (2D models of Marquardt et al. 2015), violent WD mergers (3D models of Pakmor et al. 2011, 2012 and Kromer et al. 2013, 2016), and WD-WD collisions (2D models of Kushnir 2021, private communication).

Finally, the impact of decreasing the metallicity of the progenitor WD to one half, one tenth, and one hundredth solar is shown for model N100 (dotted line). As expected, decreasing the metallicity (and hence increasing Y_c) favours the synthesis of radioactive ^{56}Ni at the expense of stable ^{58}Ni (see e.g. Timmes et al. 2003).

Kobayashi et al. (2020) recomputed the 2D delayed-detonation models of Leung & Nomoto (2018) by assuming a solar-scaled initial composition as a proxy for the progenitor metallicity. In Fig. 5, we show their $Z = 0.02$ models for three different central densities corresponding to WD masses of 1.33, 1.37, and 1.38 M_{\odot} (from low to high ^{58}Ni yield; right half-filled circles connected with a dashed line and labelled ‘zsc1’ in Table A.1). As noted in Sect. 3.1, this results in a much lower ^{22}Ne mass fraction at a given metallicity compared to what is expected from the conversion of CNO into ^{22}Ne . This largely explains the lower ^{58}Ni yields compared to the models of Seitenzahl et al. (2013). Kobayashi et al. (2020) also present the original models of Leung & Nomoto (2018) in which the ^{22}Ne mass fraction was set to the progenitor metallicity (labelled ‘zne22’ in Table A.1). In Fig. 5, we show their 1.33 M_{\odot} and 1.38 M_{\odot} models at $Z = X(^{22}\text{Ne}) = 0.02$. The ^{58}Ni yield is larger by up to a factor of three compared to the corresponding solar-scaled initial composition models (connected via a dotted line). We present models from Kobayashi et al. (2020) at different metallicities in Table A.1.

Gravitationally confined detonation (GCD): In this model, originally proposed by Plewa et al. (2004), burning is initiated as a weak central deflagration which drives a buoyant bubble of hot ash that breaks out at the stellar surface, causing a lateral acceleration and convergence of the flow of material at the opposite end. Provided the density of the compressed material is high enough, a detonation is triggered which incinerates the remainder of the WD.

In Fig. 5, we show the 3D GCD model of Seitenzahl et al. (2016) (half-filled pentagon), with a ^{58}Ni yield of 0.037 M_{\odot} for a ^{56}Ni yield of 0.742 M_{\odot} . The weak initial deflagration results in little WD pre-expansion. In this respect, it is similar to the delayed-detonation models of Seitenzahl et al. (2013) with a low number of ignition spots, where a significant amount of stable IGEs and ^{56}Ni are synthesized during the detonation phase. However, the WD does expand during the flow convergence phase, so less ^{58}Ni is synthesized compared to delayed-detonation models with similar ^{56}Ni yield.

3.5.2. Sub-Chandrasekhar-mass models

Detonations: For detonations of sub- M_{Ch} WDs the main parameter that determines the final yields is the mass of the exploding WD. The propagation of the detonation front is so fast compared to the WD expansion timescale that the density at which material is burnt is close to the original density profile

of the progenitor WD. Lower-mass WDs have lower densities at a given mass (or radial) coordinate, so the detonation produces less electron-capture isotopes than for more massive WDs. For the 1D sub- M_{Ch} models at solar metallicity shown here (SCH series of [Blondin et al. 2017](#); filled diamonds in Fig. 5), only the highest-mass WDs ($M_{\text{WD}} > 1.1 M_{\odot}$) have a ^{58}Ni yield comparable to 1D delayed-detonation models (DDC series of [Blondin et al. 2013](#)). For WD masses below $1 M_{\odot}$, the ^{58}Ni yield is significantly lower ($< 0.025 M_{\odot}$) yet not vanishingly small. Stable ^{58}Ni is still synthesized in detonations of $\lesssim 0.90 M_{\odot}$ WDs that result in low-luminosity SNe Ia (e.g. [Blondin et al. 2018](#)).

Varying the initial metallicity has the same effect as for the M_{Ch} delayed-detonation models discussed above. In the $1 M_{\odot}$ models of [Shen et al. \(2018\)](#), increasing the metallicity from solar to twice solar results in a factor of ~ 2 increase in the ^{58}Ni yield (from $7.05 \times 10^{-3} M_{\odot}$ to $1.66 \times 10^{-2} M_{\odot}$), whereas decreasing the metallicity from solar to one-half solar results in a factor of ~ 3 decrease in the ^{58}Ni yield (from $7.05 \times 10^{-3} M_{\odot}$ to $2.48 \times 10^{-3} M_{\odot}$). Similar trends are observed for the slightly super-solar ($\sim 1.6 Z_{\odot}$) $1.06 M_{\odot}$ model of [Bravo et al. \(2019\)](#) and in the extensive set of 1D sub- M_{Ch} models published by [Kushnir et al. \(2020\)](#)⁹. We note that ^{58}Ni is still synthesized at zero metallicity in these models (with a yield $\sim 10^{-3} M_{\odot}$; see Table A.1).

Several sub- M_{Ch} models at super-solar metallicities have higher ^{58}Ni (and total stable Ni) yields compared to some of the delayed-detonation models shown here, such as the $3 Z_{\odot}$ $1.06 M_{\odot}$ model of [Sim et al. \(2010\)](#)¹⁰ and the $2 Z_{\odot}$ $1.1 M_{\odot}$ model of [Kushnir et al. \(2020\)](#), which yield $\sim 0.05 M_{\odot}$ and $\sim 0.04 M_{\odot}$ of ^{58}Ni , respectively.

Double detonations: These models include a thin accreted helium layer which serves as a trigger for detonating the underlying CO core. Since the nucleosynthesis of ^{58}Ni largely occurs in the CO core, its abundance is expected to be similar to detonations of sub- M_{Ch} WDs for a given WD mass. For instance, the 2D double-detonation model of [Townsend et al. \(2019\)](#) from a $1 M_{\odot}$ WD progenitor with a $0.021 M_{\odot}$ He shell has very similar ^{56}Ni and ^{58}Ni yields compared to the $1 M_{\odot}$ solar-metallicity model of [Shen et al. \(2018\)](#). The 3D models of [Gronow et al. \(2021\)](#) display a quasi-linear trend of increasing ^{58}Ni yield with increasing ^{56}Ni mass (and hence progenitor WD mass), with a slight offset to higher ^{58}Ni yields compared to the 1D models of [Blondin et al. \(2017\)](#). For clarity we do not show the zero-metallicity models of [Gronow et al. \(2020\)](#) based on $1.05 M_{\odot}$ progenitors as they produce a cluster of points around $M(^{56}\text{Ni}) \approx 0.6 M_{\odot}$ and $M(^{58}\text{Ni}) \approx 10^{-3} M_{\odot}$, although we do include them in Table A.1. We do not show results from the 2D double-detonation models of [Fink et al. \(2010\)](#) as the corresponding abundance data is not available ([Röpke 2020](#), private communication).

Owing to their prescription for the progenitor metallicity (see Sect. 3.1), the 2D double-detonation models of [Kobayashi et al. \(2020\)](#) with solar-scaled initial composition for $Z = 0.02$

(left half-filled circles in Fig. 5 and labelled ‘zsc1’ in Table A.1) have ^{58}Ni yields of a few $10^{-3} M_{\odot}$ at most, comparable to zero-metallicity sub- M_{Ch} models published by other groups (e.g. [Sim et al. 2010](#); [Kushnir et al. 2020](#); [Gronow et al. 2020](#)). We also show their $1 M_{\odot}$ model at $Z = 0.02$ in which the ^{22}Ne mass fraction was set to the initial metallicity (i.e. $X(^{22}\text{Ne}) = 0.02$, labelled ‘zne22’ in Table A.1). The ^{58}Ni yield is one order of magnitude larger compared to the corresponding solar-scaled initial composition model (connected via a dotted line), and the total stable Ni yield is larger by a factor of ~ 3 .

Detonations in ONe WDs: In the 2D simulations carried out by [Marquardt et al. \(2015\)](#) the progenitor ONe WDs are in the mass range $1.18\text{--}1.25 M_{\odot}$ with corresponding central densities $1.0\text{--}2.0 \times 10^8 \text{ g cm}^{-3}$, which results in the production of copious amounts of ^{56}Ni ($> 0.8 M_{\odot}$). The initial composition includes ^{20}Ne but no ^{22}Ne , hence, the ^{58}Ni yield is low ($< 5 \times 10^{-3} M_{\odot}$), comparable to other zero-metallicity models shown in Fig. 5.

Violent WD mergers: In the violent merger of two sub- M_{Ch} WDs, the nucleosynthesis of IGEs occurs in similar conditions compared to detonations of single sub- M_{Ch} WDs. The secondary (accreted) WD is almost entirely burned in the process but at significantly lower densities, producing intermediate-mass elements from incomplete silicon burning and oxygen from carbon burning, while leaving some unburnt CO fuel. Of the four violent merger models with published nucleosynthesis data, solely the model of [Pakmor et al. \(2012\)](#) corresponding to the violent merger of two CO WDs of $0.9 M_{\odot}$ and $1.1 M_{\odot}$ has a significant ^{58}Ni yield ($\sim 0.028 M_{\odot}$). The other three models have either overly low metallicity ($0.9 + 0.9 M_{\odot}$ from the model of [Pakmor et al. 2011](#) at zero metallicity; $0.9 + 0.76 M_{\odot}$ model of [Kromer et al. 2016](#) at $Z = 0.01$; both yield a few times $10^{-5} M_{\odot}$ of ^{58}Ni) or reach too low a peak density during the detonation ($\rho_{\text{peak}} \lesssim 2 \times 10^6 \text{ g cm}^{-3}$ in the $0.9 + 0.76 M_{\odot}$ model of [Kromer et al. 2013](#); the ^{58}Ni yield is $\sim 0.002 M_{\odot}$).

WD-WD collisions: Following the pioneering work of [Benz et al. \(1989\)](#), several groups have performed 3D simulations of WD collisions with varying mass ratios and impact parameters ([Raskin et al. 2009, 2010](#); [Rosswog et al. 2009](#); [Lorén-Aguilar et al. 2010](#); [Hawley et al. 2012](#)). However, all of these studies consider pure CO WDs (i.e. no ^{22}Ne , equivalent to zero metallicity in our framework), and none report ^{58}Ni yields due to their use of limited nuclear reaction networks (the yield is expected to be low due to the zero metallicity, as in the 2D simulations of [Papish & Perets 2016](#) who report ^{58}Ni yields $\lesssim 0.005 M_{\odot}$ for two of their models).

Here, we show the preliminary results of 2D simulations by [Kushnir \(2021, private communication\)](#) consisting of equal-mass WD-WD collisions. From low to high ^{56}Ni yield, the WD masses are: $0.5\text{--}0.5 M_{\odot}$, $0.6\text{--}0.6 M_{\odot}$, $0.7\text{--}0.7 M_{\odot}$, $0.8\text{--}0.8 M_{\odot}$, $0.9\text{--}0.9 M_{\odot}$, and $1.0\text{--}1.0 M_{\odot}$ (not shown in Fig. 5 for clarity, although we do report its yields in Table A.1). These simulations extend the previous study of [Kushnir et al. \(2013\)](#) to include a larger 69-isotope nuclear network and solar-metallicity WDs, which results in sizeable ^{58}Ni yields ($> 10^{-2} M_{\odot}$ for collisions of WDs with masses of $0.7 M_{\odot}$ and above; see Table A.1). The detonation conditions in WD collisions are similar to those encountered in detonations of single sub- M_{Ch} WDs (as is the case for the violent WD mergers discussed above), hence, the stable ^{58}Ni yields are similar at a given ^{56}Ni mass.

⁹ We only show a subset of the 470 models presented in this study to illustrate the metallicity dependence of the ^{58}Ni yield in models with a similar setup (model IDs: 13, 49, 82, 113, 140, 157–161, 174, 210, 243, 274, 301, and 318–322). Further models with varying ^{22}Ne initial mass fraction and initial C/O ratio in the progenitor WD are reported in Table A.1, as well as models in which weak reactions are included (labelled ‘CIWD_NNNw’; the impact on the stable Ni yields is negligible).

¹⁰ The other models of [Sim et al. \(2010\)](#) are at zero metallicity, and, hence their ^{58}Ni yield is less than $0.002 M_{\odot}$.

3.5.3. Summary

The M_{Ch} and sub- M_{Ch} models studied here clearly occupy distinct regions of the $M(^{56}\text{Ni})$ - $M(^{58}\text{Ni})$ parameter space shown in Fig. 5. At a given ^{56}Ni yield, and for the same initial metallicity, sub- M_{Ch} models synthesize less ^{58}Ni compared to M_{Ch} models.

Typical ^{58}Ni yields are 0–0.03 M_{\odot} for sub- M_{Ch} models and 0.02–0.08 M_{\odot} for M_{Ch} models (except for the weakest M_{Ch} deflagration models N1def and N3def of Fink et al. 2014 which synthesize around 0.01 M_{\odot} of ^{58}Ni). This is modulated by the progenitor metallicity and central density of the exploding WD. In particular, reducing the central density by a factor of ~ 3 results in a $\sim 50\%$ decrease in the ^{58}Ni yield in the delayed-detonation model N100 of Seitenzahl et al. (2013) and the pure deflagration model N100def of Fink et al. (2014). The synthesis of ^{58}Ni does not necessarily require burning at the highest central densities of M_{Ch} WD progenitors. The highest-mass ($M_{\text{WD}} > 1 M_{\odot}$) sub- M_{Ch} progenitors have ^{58}Ni yields comparable to some of the M_{Ch} models shown in Fig. 5, and sometimes even higher for super-solar metallicity progenitors.

The trend remains the same if we take into account the total stable nickel yield as opposed to solely ^{58}Ni . However, the double-detonation models of Gronow et al. (2021) synthesize a significant fraction of stable Ni in the form of ^{60}Ni (20–30%) and ^{62}Ni ($\lesssim 10\%$), and the double-detonation model of Townsley et al. (2019) yields $\sim 45\%$ of stable Ni as ^{60}Ni , which causes these models to overlap with the 1D M_{Ch} delayed-detonation models of Blondin et al. (2013). Likewise, the zero-metallicity double-detonation models of Gronow et al. (2020) synthesize up to $\sim 90\%$ of their stable Ni as ^{60}Ni , resulting in an order of magnitude increase in their stable Ni yields ($> 10^{-2} M_{\odot}$) compared to their ^{58}Ni yields ($< 2 \times 10^{-3} M_{\odot}$; see Table A.1).

When considering the formation of [Ni II] lines in late-time SN Ia spectra (~ 200 d past explosion in what follows), it is the total stable Ni abundance at that time that matters. This abundance is essentially set within the first day after the explosion, as the sole decay chains with longer half-lives ($^{60}\text{Fe} \rightarrow ^{60}\text{Co} \rightarrow ^{60}\text{Ni}$; see Table 1) only contribute $\lesssim 10^{-4} M_{\odot}$ of the total decayed stable Ni yield. In the following section, we explore whether the lower abundance of stable Ni in sub- M_{Ch} models alone can explain the predicted lack of [Ni II] lines in their late-time spectra.

4. Impact of stable Ni abundance and ionization on nebular [Ni II] lines

4.1. The absence of [Ni II] lines from sub- M_{Ch} models

In Blondin et al. (2018), we concluded that the key parameter in determining the presence of [Ni II] lines in the late-time spectrum of our low-luminosity M_{Ch} model DDC25 was larger abundance of stable Ni by a factor of ~ 17 , compared to its sub- M_{Ch} counterpart SCH2p0 ($2.9 \times 10^{-2} M_{\odot}$ in the M_{Ch} model cf. $1.7 \times 10^{-3} M_{\odot}$ in the sub- M_{Ch} model; see Table A.1). However, we also noted that the lower Ni ionization (i.e. higher Ni II/Ni III ratio) in the inner ejecta of the M_{Ch} model further enhanced their strength (Fig. 6, thin dashed line), while the low Ni II/Ni III ratio in the sub- M_{Ch} model completely suppressed both lines (Fig. 6, thin solid line; see also Wilk et al. 2018).

We further explore the relative impact of abundance versus ionization on the strength of [Ni II] lines in late-time spectra by considering M_{Ch} and sub- M_{Ch} models at the high-luminosity end, where the differences in stable Ni yield are less pronounced (see Fig. 5). For this, we use the M_{Ch} delayed-detonation model DDC0 and the sub- M_{Ch} detonation model SCH7p0 (resulting

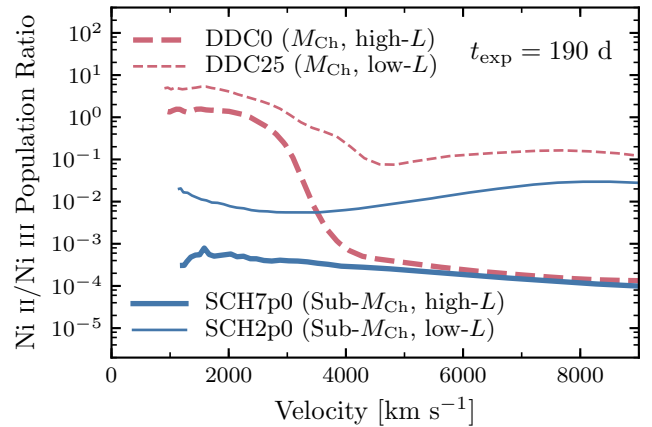


Fig. 6. Ni II/Ni III population ratio at 190 d past explosion for the high-luminosity models DDC0 (M_{Ch} ; thick dashed line) and SCH7p0 (sub- M_{Ch} ; thick solid line) as well as the low-luminosity models DDC25 (M_{Ch} ; thin dashed line) and SCH2p0 (sub- M_{Ch} ; thin solid line). Regardless of the luminosity, Ni III dominates in the sub- M_{Ch} models all the way to the innermost ejecta ($\lesssim 3000 \text{ km s}^{-1}$), whereas Ni II dominates there in the M_{Ch} models.

from the detonation of a $1.15 M_{\odot}$ WD progenitor), both of which have a ^{56}Ni yield of $\sim 0.84 M_{\odot}$. Unlike the aforementioned low-luminosity models, the stable Ni yield is comparable in both models ($4.7 \times 10^{-2} M_{\odot}$ in the M_{Ch} model cf. $3.3 \times 10^{-2} M_{\odot}$ for the sub- M_{Ch} model).

Despite the similar stable Ni abundance, however, the ionization profiles greatly differ and show the same behaviour as for the low-luminosity models: Ni II dominates in the inner ejecta of the M_{Ch} model (Fig. 6, thick dashed line), whereas Ni III dominates in the sub- M_{Ch} model (Fig. 6, thick solid line). As a result, the M_{Ch} model displays prominent [Ni II] lines in its late-time spectrum, while the sub- M_{Ch} model shows no such lines, as was the case for the low-luminosity models (Fig. 7).

The higher Ni ionization in the sub- M_{Ch} models is a result of their factor of 3–4 lower density in the inner $\sim 3000 \text{ km s}^{-1}$, which both lowers the Ni III \rightarrow II recombination rate and increases the deposited decay energy per unit mass. The presence of ^{56}Ni (which has all decayed to ^{56}Co at 190 d past explosion) down to the central layers in these sub- M_{Ch} models causes the local deposition of positron kinetic energy from ^{56}Co decay to partly compensate for the less efficient trapping of γ -rays: 40–50% of the deposited decay energy below 3000 km s^{-1} is from positrons in both models (see also Wilk et al. 2018).

4.2. Impact of the Ni II/Ni III ratio on [Ni II] lines

The presence of [Ni II] lines thus appears to be mostly related to an ionization effect. We illustrate this by artificially increasing the Ni II/Ni III ratio (hence, decreasing the ionization) of the sub- M_{Ch} models below 3000 km s^{-1} , while keeping the original stable Ni abundance and temperature profiles the same (see Appendix C for details on the numerical procedure).

The dominant formation mechanism for these lines is collisional excitation, hence, their strength scales with the Ni II population density. As a result, [Ni II] lines do indeed emerge in both the high-luminosity sub- M_{Ch} model (in which the stable Ni yield was similar to the corresponding M_{Ch} model) and the low-luminosity sub- M_{Ch} model (in which the stable Ni yield was a factor of ~ 17 lower than in the M_{Ch} model). Despite being

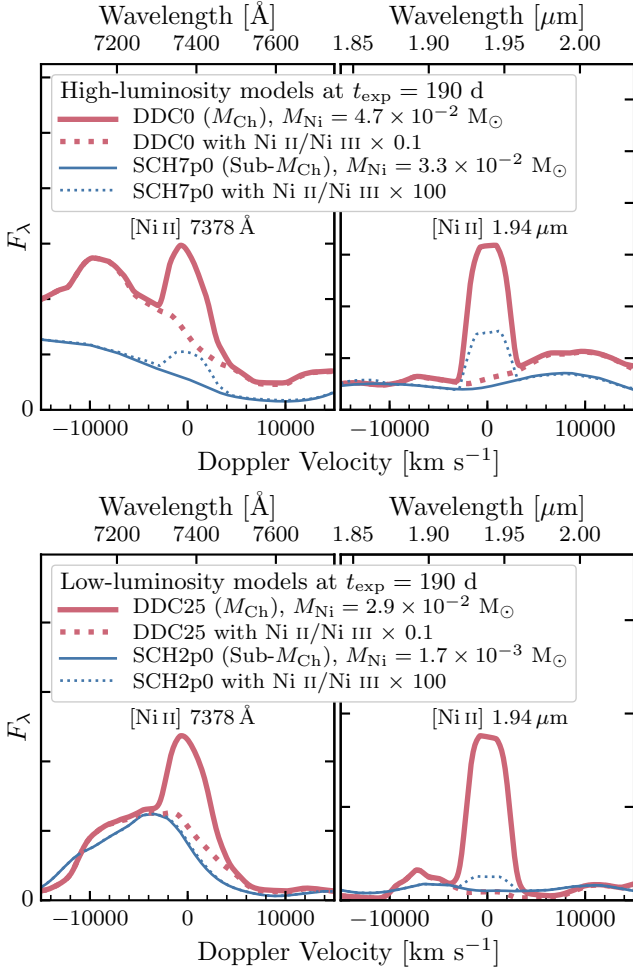


Fig. 7. Top panel: Optical (left) and near-infrared (right) [Ni II] line profiles at 190 d past explosion in the high-luminosity models DDC0 (M_{Ch} ; thick solid line) and SCH7p0 (sub- M_{Ch} ; thin solid line). The dotted lines show the impact of artificially decreasing (increasing) the Ni II/Ni III ratio on the emergence of [Ni II] lines in the M_{Ch} (sub- M_{Ch}) model. The near-infrared (NIR) line profiles were normalized to the same mean flux in the range 1.87–1.88 μm ; the optical profiles are not normalized. Bottom panel: Same as above for the low-luminosity models DDC25 (M_{Ch} ; thick solid line) and SCH2p0 (sub- M_{Ch} ; thin solid line). We note the absence of an optical [Ni II] 7378 Å line in the sub- M_{Ch} model with high Ni II/Ni III ratio see text for details).

about six times stronger than the NIR line¹¹, the optical [Ni II] 7378 Å line only manages to produce a small excess flux in the low-luminosity sub- M_{Ch} model SCH2p0, as it is swamped by the neighbouring [Ca II] 7300 Å doublet. This does not occur in the high-luminosity sub- M_{Ch} model SCH7p0 due to the lower Ca abundance in the inner ejecta of this model ($X(\text{Ca}) < 10^{-7}$ below 5000 km s^{-1} cf. 5–6 $\times 10^{-2}$ in the low-luminosity model SCH2p0).

Nonetheless, the emergent [Ni II] lines in our sub- M_{Ch} models remain comparatively weak compared to those in the M_{Ch} models, even when the Ni II/Ni III ratio is increased by a factor of 100. This is particularly true for the low-luminosity sub- M_{Ch} model SCH2p0, which suggests that a Ni abundance of at least $10^{-2} M_{\odot}$ is needed to form strong [Ni II] lines. This seemingly

excludes sub- M_{Ch} progenitors for low-luminosity SNe Ia presenting strong [Ni II] lines in their late-time spectra, at least in solar-metallicity environments.

The question remains whether a physical mechanism exists to boost the Ni II/Ni III ratio in the inner ejecta of sub- M_{Ch} models, which would cause [Ni II] lines to emerge despite the low Ni abundance. One possible mechanism is clumping: the higher density in the clumps enhances the recombination rate, hence, reducing the average ionization. Clumping is expected to result from hydrodynamical instabilities during the initial deflagration phase of M_{Ch} delayed-detonation models (e.g. Golombek & Niemeyer 2005). However, such instabilities are not predicted in sub- M_{Ch} detonation models (e.g. García-Senz et al. 1999). Mazzali et al. (2020) has suggested that clumping could also develop at much later times (~ 1.5 yr after explosion in their model for SN 2014J) through the development of local magnetic fields, which could also occur in sub- M_{Ch} ejecta. Clumping could also develop on an intermediate timescale of days via the ^{56}Ni bubble effect (e.g. Wang 2005). Regardless of its physical origin, Wilk et al. (2020) found that clumping indeed lowers the average ionization in the inner ejecta but not enough to produce a Ni II/Ni III ratio favourable for the appearance of [Ni II] lines, even for a volume-filling factor $f = 0.1$, which results in a ten-fold increase of the density in the clumps.

Conversely, artificially decreasing the Ni II/Ni III ratio (hence, increasing the Ni ionization) of the M_{Ch} models by a factor of 10 (while keeping the original stable Ni abundance the same) completely suppresses both the optical and near-infrared [Ni II] lines (Fig. 7, thick dotted lines). We stress that this procedure is for illustrative purposes only since we do not compute a proper radiative-transfer solution (in particular the temperature profile is left unchanged, as are the population densities of all other species). In the following section, we investigate how inward mixing of ^{56}Ni , as predicted in 3D delayed-detonation models, could affect the appearance of [Ni II] lines in M_{Ch} models.

5. Impact of mixing on nebular [Ni II] lines

5.1. Macroscopic versus microscopic mixing

Macroscopic mixing in SNe Ia occurs during the deflagration phase of 3D M_{Ch} delayed-detonation models, due to rising bubbles of buoyant hot nuclear ash and downward mixing of nuclear fuel (e.g. Seitenzahl et al. 2013). In the innermost ejecta, stable IGEs can be transported outwards while ^{56}Ni synthesized at higher velocities is mixed inwards. As a result, there is no radial chemical segregation between stable IGEs and ^{56}Ni -rich layers as in the 1D M_{Ch} models studied here. While it is not possible to simulate such macroscopic mixing in 1D, where the composition is fixed at a given radial (or velocity) coordinate, various numerical techniques have been developed to approximate this and other multi-dimensional effects (see e.g. Duffell 2016; Zhou 2017; Mabanta & Murphy 2018; Mabanta et al. 2019; Dessart & Hillier 2020).

Instead, a commonly used expedient in 1D consists in homogenizing the composition in successive mass shells by applying a running boxcar average (e.g. Woosley et al. 2007; Dessart et al. 2014). In this approach, the mixing is both macroscopic (material is effectively advected to larger and lower velocities) and microscopic (the composition is completely homogenized within each mass shell at each step of the running average). The method is convenient but results in non-physical composition profiles that affect the spectral properties (e.g. Dessart & Hillier

¹¹ Since both transitions share the same upper level (Table B.1; see also Flörs et al. 2020), the ratio of the emergent flux in each line only depends on the ratio of $\Delta E A_{ul}$, where ΔE is the transition energy and A_{ul} is the Einstein coefficient for spontaneous emission.

2020). We note that numerical diffusion causes some level of microscopic mixing even in 3D simulations.

Here, we simply wish to illustrate the impact of mixing on the strength of [Ni II] lines in late-time spectra of the M_{Ch} delayed-detonation model DDC15 of Blondin et al. (2015). For this, we adopt a fully microscopic mixing approach by homogenizing the composition in the inner ejecta below some cutoff velocity v_{mix} . In what follows, we refer to this as ‘uniform’ mixing. The mass fraction of a given species i is set to its mass-weighted-average for $v \leq v_{\text{mix}}$, and is left unchanged for $v > v_{\text{orig}} = v_{\text{mix}} + \Delta v_{\text{trans}}$, where $\Delta v_{\text{trans}} = \{500, 1000\} \text{ km s}^{-1}$. To avoid strong compositional discontinuities at v_{mix} , we use a cosine function to smoothly transition from the uniform to the unchanged composition over the interval $[v_{\text{mix}}, v_{\text{orig}}]$. Formally, in each mass shell with velocity coordinate v :

$$X_i(v) = \begin{cases} \frac{\sum_{v' < v_{\text{mix}}} X_i(v') \Delta M(v')}{\sum_{v' < v_{\text{mix}}} \Delta M(v')} & \text{for } v < v_{\text{mix}}, \\ X_i(v_{\text{mix}}) + f_{\cos} X_i(v_{\text{orig}}) & \text{for } v_{\text{mix}} \leq v < v_{\text{orig}}, \\ X_i(v) \text{ (unchanged)} & \text{for } v \geq v_{\text{orig}}. \end{cases} \quad (3)$$

where

$$f_{\cos} = \frac{1}{2} \left\{ 1 - \cos \left[\left(\frac{v - v_{\text{mix}}}{\Delta v_{\text{trans}}} \right) \pi \right] \right\}. \quad (4)$$

This procedure conserves the total mass of each species as the density profile is left unchanged.

The resulting Ni abundance profiles at 190 d past explosion are shown in Fig. 8 for values of $v_{\text{mix}} = 3750, 5000, 7500$, and 15000 km s^{-1} (top panel). The angle-averaged profile of the 3D delayed-detonation model N100 of Seitenzahl et al. (2013) illustrates the advection of stable Ni to larger velocities (grey dashed line), resulting in a stable Ni mass fraction $\sim 5 \times 10^{-2}$ below $\sim 4000 \text{ km s}^{-1}$, as in our $v_{\text{mix}} = 7500 \text{ km s}^{-1}$ model.

5.2. Impact of mixing on ionization and [Ni II] lines

The uniform mixing we apply not only affects the abundance profiles, but the ionization as well (Fig. 8, bottom panel). In the inner 3000 km s^{-1} , the Ni II/Ni III ratio systematically decreases with increasing v_{mix} . This increase in ionization simply traces the increase in deposited energy from radioactive decays, through inward mixing of ^{56}Co (see inset). Unlike the comparison between M_{Ch} and sub- M_{Ch} models in the previous section, here the density profile is identical for all uniformly mixed models, such that the ^{56}Co radioactive decay heating (20-25% of which is due to local deposition of positron kinetic energy below $\sim 3000 \text{ km s}^{-1}$) predominantly determines the ionization state.

Variations in the amount of cooling through line emission further affect the energy balance. This is best seen in the mixed model with $v_{\text{mix}} = 15000 \text{ km s}^{-1}$, where the Ni II/Ni III ratio below $\sim 4000 \text{ km s}^{-1}$ is comparable to the $v_{\text{mix}} = 7500 \text{ km s}^{-1}$ model despite the $\sim 20\%$ lower decay heating¹². This is due to the less efficient line cooling in the $v_{\text{mix}} = 15000 \text{ km s}^{-1}$ model (where [Ca II] collisional cooling dominates due to the larger Ca mass fraction in these layers) compared to the $v_{\text{mix}} = 7500 \text{ km s}^{-1}$ model, in which cooling via [Fe II] and [Fe III] transitions is more efficient.

¹² The mass fraction of ^{56}Co is ~ 0.08 for the $v_{\text{mix}} = 15000 \text{ km s}^{-1}$ model cf. ~ 0.11 for the $v_{\text{mix}} = 7500 \text{ km s}^{-1}$ model in those layers.

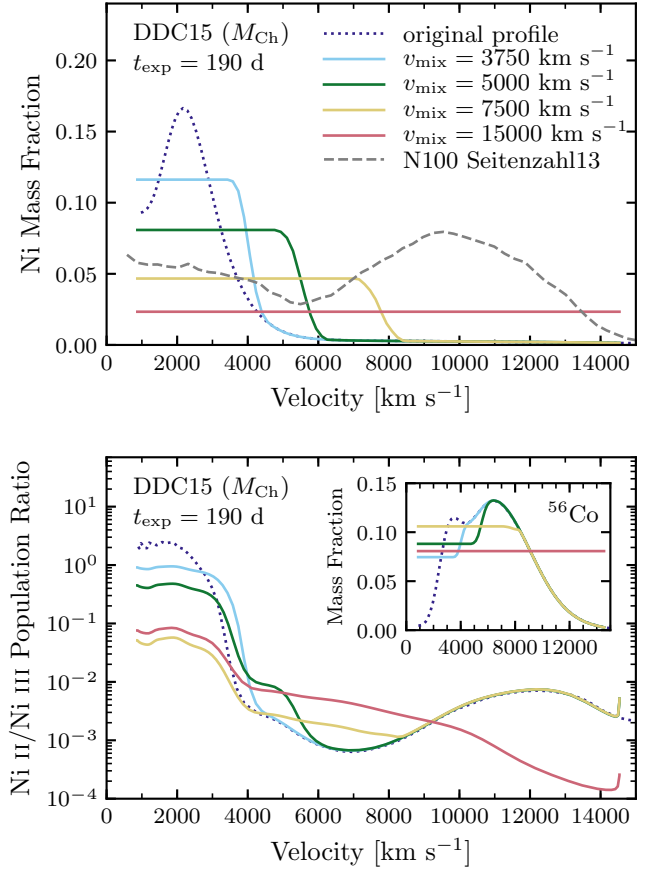


Fig. 8. Impact of uniformly mixing the composition within a cutoff velocity $v_{\text{mix}} = 3750, 5000, 7500$, and 15000 km s^{-1} on the Ni abundance profile (top) and Ni II/Ni III population ratio (bottom), illustrated using the M_{Ch} delayed-detonation model DDC15 of Blondin et al. (2015) at 190 d past explosion. The stable Ni mass for this model is $\sim 0.03 M_{\odot}$ (see Table A.1). We show the angle-averaged Ni abundance profile of the 3D delayed-detonation model N100 of Seitenzahl et al. (2013) for comparison (grey dashed line, top panel). The inset in the lower panel shows the ^{56}Co abundance profiles, whose decay heating by positrons and γ -rays largely determines the ionization state at this time.

The resulting [Ni II] line profiles are shown in Fig. 9. As expected, the [Ni II] $1.94 \mu\text{m}$ line is only present in models where the Ni II/Ni III ratio fraction is sufficiently high ($> 10^{-1}$, that is, for $v_{\text{mix}} = 3750$ and 5000 km s^{-1} , as well as in the original DDC15 model), and its strength is modulated by the abundance of Ni in the line-formation region. Thus, the $v_{\text{mix}} = 3750 \text{ km s}^{-1}$ model displays a stronger [Ni II] $1.94 \mu\text{m}$ line compared to the original DDC15 model since the Ni mass fraction below $\sim 1500 \text{ km s}^{-1}$ is higher. The FWHM of the line is also slightly larger ($\sim 4500 \text{ km s}^{-1}$ cf. $\sim 4250 \text{ km s}^{-1}$ for the original profile) due to the larger radial extension of the line-emission region. For $v_{\text{mix}} = 5000 \text{ km s}^{-1}$, the [Ni II] $1.94 \mu\text{m}$ line is weaker than in the original unmixed model owing to the lower Ni mass fraction below $\sim 3500 \text{ km s}^{-1}$. However, its FWHM is similar despite the presence of stable Ni beyond 4000 km s^{-1} , since the Ni II/Ni III ratio drops below 10^{-1} in these layers.

This trend holds for the optical [Ni II] 7378 \AA line but is more difficult to discern, as the [Ca II] 7300 \AA doublet progressively emerges with increasing v_{mix} . A weak [Ni II] 7378 \AA line is indeed present in the original DDC15 and in the $v_{\text{mix}} = 3750 \text{ km s}^{-1}$ models, where the Ca mass fraction is $< 10^{-2}$ below $\sim 3000 \text{ km s}^{-1}$. In the other models, inward mixing of Ca

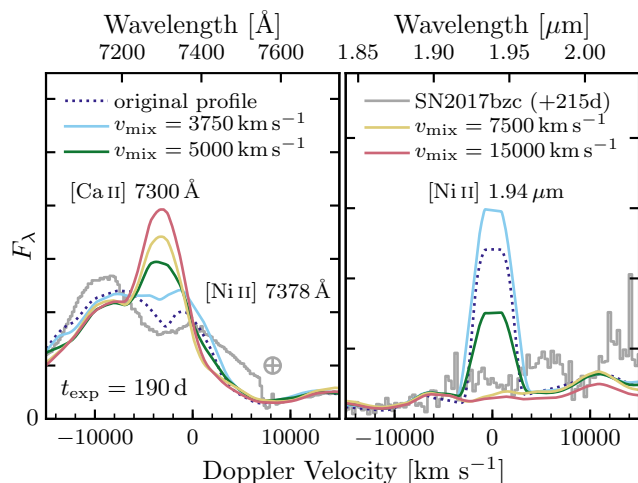


Fig. 9. Impact of uniform mixing on the optical (left) and near-infrared (right) [Ni II] line profiles at 190 d past explosion, using the same models as in Fig. 8. Also shown are observations of SN 2017bzc at a slightly later phase (+215 d past maximum) scaled to match the mean flux of the original profile in the range 7600–8000 Å and 1.83–1.91 μm, respectively (grey line). The feature marked with a ‘⊕’ at +8000 km s^{−1} in the optical spectrum is due to absorption by the Earth’s atmosphere (A-band).

results in a mass fraction of a few times 10^{-2} which is sufficient to swamp the [Ni II] 7378 Å line, as [Ca II] becomes a dominant coolant. The overabundance of Ca in the inner ejecta illustrates a severe limitation of our 1D approach to mixing: in the 3D delayed-detonation model N100 of Seitzzahl et al. (2013), the Ca mass fraction remains almost systematically $\lesssim 10^{-5}$ below 5000 km s^{−1} in all directions (Seitzzahl 2021, private communication).

Furthermore, aside from low-luminosity 91bg-like events, the presence of [Ca II] 7300 Å in late-time spectra is not compatible with observations of SNe Ia, as illustrated with SN 2017bzc in the left panel of Fig. 9 (grey line, Flörs et al. 2020; see also Maguire et al. 2018). Our original (unmixed) DDC15 model does not predict significant [Ca II] 7300 Å emission (dotted line): The broad double-humped feature around 7300 Å is dominated by [Ni II] 7378 Å to the red and [Fe II] 7155 Å to the blue (as noted by Flörs et al. 2020). However, our model clearly overestimates the strength of [Ni II] 1.94 μm, and while we can adjust the level of mixing to match its strength, this inevitably results in an overestimation of [Ca II] 7300 Å in the optical.

Our results nonetheless suggest that inward mixing of ^{56}Ni can completely wash out otherwise strong [Ni II] lines in late-time spectra of M_{Ch} models. A more physical treatment of mixing could result in pockets rich in stable nickel being physically isolated from regions rich in ^{56}Ni (as in the 3D delayed-detonation models of Bravo & García-Senz 2008). This would suppress decay heating of the stable Ni pockets by local positron kinetic energy deposition from ^{56}Co decay, and compensate in part for the increase in ionization. Moreover, such stable Ni pockets could be moderately compressed through the ^{56}Ni bubble effect (e.g. Wang 2005; Dessart et al. 2021), enhancing the Ni recombination rate. Whatever the exact effect, mixing complicates the use of [Ni II] lines to constrain the stable Ni abundance, and the absence of these lines cannot be unambiguously associated with a sub- M_{Ch} explosion.

6. Conclusions

We studied the explosive nucleosynthesis of stable nickel and its dominant isotope ^{58}Ni in SNe Ia to test its use as a diagnostic of the progenitor WD mass. Among all reactions ending in ^{58}Ni , we find that the radiative proton-capture reaction $^{57}\text{Co}(p, \gamma)^{58}\text{Ni}$ mostly determines the final ^{58}Ni abundance in both M_{Ch} and sub- M_{Ch} models. Contrary to expectations, direct α captures on ^{54}Fe only contribute at the percent level to the net nucleosynthetic flux to ^{58}Ni , even in the α -rich freeze-out regime from nuclear statistical equilibrium.

At solar metallicity and for a given ^{56}Ni yield, sub- M_{Ch} models synthesize less ^{58}Ni (~ 0 – $0.03 M_{\odot}$) compared to M_{Ch} models (~ 0.02 – $0.08 M_{\odot}$), although this difference is reduced for WD masses $\gtrsim 1 M_{\odot}$ or for super-solar metallicities. The trend remains the same when considering the total stable nickel yield as opposed to only ^{58}Ni , although some double-detonation models synthesize 30–90% of stable Ni in the form of heavier isotopes (in particular ^{60}Ni), causing an overlap with the 1D M_{Ch} delayed-detonation models studied here.

The systematic absence of [Ni II] lines in late-time spectra of sub- M_{Ch} models is due to the higher Ni ionization in the inner ejecta, where Ni III dominates over Ni II. This higher ionization results from the lower density of the inner ejecta compared to M_{Ch} models, which limits the Ni III \rightarrow II recombination rate and increases the deposited decay energy per unit mass. In 1D M_{Ch} models, the difference in ionization is exacerbated by the underabundance of ^{56}Ni in the inner ejecta, which results in lower local kinetic energy deposition by positrons from ^{56}Co decay at late times.

Artificially reducing the Ni ionization of the sub- M_{Ch} models (while maintaining the same Ni abundance) results in the emergence of [Ni II] lines, although these remain fairly weak in low-luminosity models where the stable Ni yield is $< 10^{-2} M_{\odot}$, even when the Ni II/Ni III ratio is increased by a factor of 100. Any mechanism that reduces the ionization state of the inner ejecta in sub- M_{Ch} models could thus in principle lead to the formation of [Ni II] lines, thereby invalidating the use of this line as a fool-proof discriminant between M_{Ch} and sub- M_{Ch} explosions. One such mechanism is clumping, although a recent study by Wilk et al. (2020) showed that the ionization level was not lowered sufficiently to produce a favourable Ni II/Ni III ratio, at least in their 1D implementation of clumping via volume-filling factors.

Likewise, an increase in the Ni ionization of the M_{Ch} models through a tenfold reduction of the Ni II/Ni III ratio completely suppresses both optical and near-infrared [Ni II] lines, despite a relatively large abundance of stable Ni (3 – $5 \times 10^{-2} M_{\odot}$). This again demonstrates the importance of ionization overabundance in determining the presence of [Ni II] lines in late-time spectra of M_{Ch} models.

Conversely, mixing can completely wash out otherwise strong [Ni II] lines in M_{Ch} models. Our investigation of this effect in 1D is artificial, but nonetheless captures the main effect of the inward microscopic mixing of ^{56}Ni and the resulting increase in decay energy deposition and, hence, the Ni ionization state, in the inner ejecta. At the same time, stable Ni is mixed outwards, reducing its abundance in the [Ni II] line-formation region. A more elaborate treatment of mixing could mitigate in part this increase in Ni ionization.

In summary, the presence of [Ni II] lines in late-time spectra of SNe Ia is largely the result of a favourable Ni ionization state in the inner ejecta and it is not guaranteed solely based on a large abundance of stable nickel. This sensitivity to ionization complicates the use of these lines alone as a diagnostic of the progenitor

WD mass (or simply differentiating between M_{Ch} and sub- M_{Ch} ejecta). It is possible that [Ni II] lines in combination with other lines of [Co II/III] and [Fe II/III] present in late-time spectra could help constrain the Ni ionization state. In that case, a low Ni ionization combined with an absence of [Ni II] lines would point to a very low abundance of stable nickel ($\lesssim 10^{-3} M_{\odot}$) and, in turn, to a sub- M_{Ch} progenitor. Conversely, the presence of strong [Ni II] lines in a low-luminosity SN Ia would likely be the result of a Chandrasekhar-mass explosion.

Acknowledgements. The authors acknowledge useful discussions with Subo Dong, Chiaki Kobayashi, Doron Kushnir, Kate Maguire, Fritz Röpke, Ivo Seitenzahl, Ken Shen, Kanji Mori, Dean Townsley, and members of the Garching SN group (in particular: Andreas Flörs, Bruno Leibundgut, Rüdiger Pakmor, Jason Spyromilio, and Stefan Taubenberger). SB thanks Inma Domínguez for performing the stellar-evolution calculation for model 5p0_Z0p014, Chiaki Kobayashi and Shing Chi Leung for sending the tabulated yields from Kobayashi et al. (2020), and Doron Kushnir for sending the nickel yields from his 2D equal-mass WD-WD collision models ahead of publication. This work was supported by the ‘Programme National de Physique Stellaire’ (PNPS) of CNRS/INSU co-funded by CEA and CNES. This research was supported by the Excellence Cluster ORIGINS which is funded by the Deutsche Forschungsgemeinschaft (DFG, German Research Foundation) under Germany’s Excellence Strategy EXC-2094-390783311. SB acknowledges support from the ESO Scientific Visitor Programme in Garching. EB’s research is supported by MINECO grant PGC2018-095317-B-C21. FXT’s research is partially supported by the NSF under grant No. PHY-1430152 for the Physics Frontier Center Joint Institute for Nuclear Astrophysics Center for the Evolution of the Elements (JINA-CEE). DJH thank NASA for partial support through theory grants NNX14AB41G and 80NSSC20K0524. This research has made use of computing facilities operated by CeSAM data centre at LAM, Marseille, France. This work made use of the Heidelberg Supernova Model Archive (HESMA), <https://hesma.h-its.org>.

References

- Arnett, W. D. 1982, *ApJ*, 253, 785
- Asplund, M., Grevesse, N., Sauval, A. J., & Scott, P. 2009, *ARA&A*, 47, 481
- Benz, W., Hills, J. G., & Thielemann, F. K. 1989, *ApJ*, 342, 986
- Blondin, S., Dessart, L., & Hillier, D. J. 2015, *MNRAS*, 448, 2766
- Blondin, S., Dessart, L., & Hillier, D. J. 2018, *MNRAS*, 474, 3931
- Blondin, S., Dessart, L., Hillier, D. J., & Khokhlov, A. M. 2013, *MNRAS*, 429, 2127
- Blondin, S., Dessart, L., Hillier, D. J., & Khokhlov, A. M. 2017, *MNRAS*, 470, 157
- Bravo, E. 2019, *A&A*, 624, A139
- Bravo, E., Badenes, C., & Martínez-Rodríguez, H. 2019, *MNRAS*, 482, 4346
- Bravo, E., Domínguez, I., Badenes, C., Piersanti, L., & Straniero, O. 2010, *ApJ*, 711, L66
- Bravo, E. & García-Senz, D. 2008, *A&A*, 478, 843
- Cabezon, R. M., García-Senz, D., & Bravo, E. 2004, *ApJS*, 151, 345
- Chamulak, D. A., Brown, E. F., Timmes, F. X., & Dupczak, K. 2008, *ApJ*, 677, 160
- Chu, S. Y. F., Ekström, L. P., & Firestone, R. B. 1999, *WWW Table of Radioactive Isotopes*, database version 1999-02-28
- Clifford, F. E. & Tayler, R. J. 1965, *MmRAS*, 69, 21
- Dessart, L., Blondin, S., Hillier, D. J., & Khokhlov, A. 2014, *MNRAS*, 441, 532
- Dessart, L. & Hillier, D. J. 2020, *A&A*, 643, L13
- Dessart, L., John Hillier, D., Sukhbold, T., Woosley, S. E., & Janka, H. T. 2021, *A&A*, 652, A64
- Dhawan, S., Flörs, A., Leibundgut, B., et al. 2018, *A&A*, 619, A102
- Dong, S., Katz, B., Kushnir, D., & Prieto, J. L. 2015, *MNRAS*, 454, L61
- Duffell, P. C. 2016, *ApJ*, 821, 76
- Fink, M., Kromer, M., Seitenzahl, I. R., et al. 2014, *MNRAS*, 438, 1762
- Fink, M., Röpke, F. K., Hillebrandt, W., et al. 2010, *A&A*, 514, A53
- Flörs, A., Spyromilio, J., Maguire, K., et al. 2018, *A&A*, 620, A200
- Flörs, A., Spyromilio, J., Taubenberger, S., et al. 2020, *MNRAS*, 491, 2902
- García-Senz, D., Bravo, E., & Woosley, S. E. 1999, *A&A*, 349, 177
- Golombek, I. & Niemeyer, J. C. 2005, *A&A*, 438, 611
- Gronow, S., Collins, C., Ohlmann, S. T., et al. 2020, *A&A*, 635, A169
- Gronow, S., Collins, C. E., Sim, S. A., & Röpke, F. K. 2021, *A&A*, 649, A155
- Hartmann, D., Woosley, S. E., & El Eid, M. F. 1985, *ApJ*, 297, 837
- Hawley, W. P., Athanassiadou, T., & Timmes, F. X. 2012, *ApJ*, 759, 39
- Hillier, D. J. & Dessart, L. 2012, *MNRAS*, 424, 252
- Hut, P. & Inagaki, S. 1985, *ApJ*, 298, 502
- Jha, S. W., Maguire, K., & Sullivan, M. 2019, *Nature Astronomy*, 3, 706
- Katz, B. & Dong, S. 2012, *arXiv e-prints*, arXiv:1211.4584
- Khatami, D. K. & Kasen, D. N. 2019, *ApJ*, 878, 56
- Kobayashi, C., Leung, S.-C., & Nomoto, K. 2020, *ApJ*, 895, 138
- Kromer, M., Fremling, C., Pakmor, R., et al. 2016, *MNRAS*, 459, 4428
- Kromer, M., Pakmor, R., Taubenberger, S., et al. 2013, *ApJ*, 778, L18
- Kushnir, D., Katz, B., Dong, S., Livne, E., & Fernández, R. 2013, *ApJ*, 778, L37
- Kushnir, D., Wygoda, N., & Sharon, A. 2020, *MNRAS*, 499, 4725
- Lach, F., Röpke, F. K., Seitenzahl, I. R., et al. 2020, *A&A*, 644, A118
- Leung, S.-C. & Nomoto, K. 2018, *ApJ*, 861, 143
- Livio, M. & Mazzali, P. 2018, *Phys. Rep.*, 736, 1
- Lodders, K. 2003, *ApJ*, 591, 1220
- Lorén-Aguilar, P., Isern, J., & García-Berro, E. 2010, *MNRAS*, 406, 2749
- Mabanta, Q. A. & Murphy, J. W. 2018, *ApJ*, 856, 22
- Mabanta, Q. A., Murphy, J. W., & Dolence, J. C. 2019, *ApJ*, 887, 43
- Magee, M. R., Maguire, K., Kotak, R., & Sim, S. A. 2021, *MNRAS*, 502, 3533
- Magkotsios, G., Timmes, F. X., Hungerford, A. L., et al. 2010, *ApJS*, 191, 66
- Maguire, K., Sim, S. A., Shingles, L., et al. 2018, *MNRAS*, 477, 3567
- Maoz, D. & Mannucci, F. 2012, *PASA*, 29, 447
- Marquardt, K. S., Sim, S. A., Ruiter, A. J., et al. 2015, *A&A*, 580, A118
- Martínez-Rodríguez, H., Piro, A. L., Schwab, J., & Badenes, C. 2016, *ApJ*, 825, 57
- Mazzali, P. A., Bikmaev, I., Sunyaev, R., et al. 2020, *MNRAS*, 494, 2809
- Mori, K., Famiano, M. A., Kajino, T., et al. 2018, *ApJ*, 863, 176
- Nadyozhin, D. K. & Yudin, A. V. 2004, *Astronomy Letters*, 30, 634
- Nomoto, K. & Kondo, Y. 1991, *ApJ*, 367, L19
- Nomoto, K., Thielemann, F.-K., & Yokoi, K. 1984, *ApJ*, 286, 644
- Pakmor, R., Hachinger, S., Röpke, F. K., & Hillebrandt, W. 2011, *A&A*, 528, A117+
- Pakmor, R., Kromer, M., Röpke, F. K., et al. 2010, *Nature*, 463, 61
- Pakmor, R., Kromer, M., Taubenberger, S., et al. 2012, *ApJ*, 747, L10
- Papish, O. & Perets, H. B. 2016, *ApJ*, 822, 19
- Piersanti, L., Bravo, E., Cristallo, S., et al. 2017, *ApJ*, 836, L9
- Pinto, P. A. & Eastman, R. G. 2000, *ApJ*, 530, 744
- Piro, A. L. & Bildsten, L. 2008, *ApJ*, 673, 1009
- Piro, A. L., Chang, P., & Weinberg, N. N. 2010, *ApJ*, 708, 598
- Plewa, T., Calder, A. C., & Lamb, D. Q. 2004, *ApJ*, 612, L37
- Quinet, P. & Le Dourneuf, M. 1996, *A&AS*, 119, 99
- Raskin, C., Scannapieco, E., Rockefeller, G., et al. 2010, *ApJ*, 724, 111
- Raskin, C., Timmes, F. X., Scannapieco, E., Diehl, S., & Fryer, C. 2009, *MNRAS*, 399, L156
- Rosswog, S., Kasen, D., Guillochon, J., & Ramirez-Ruiz, E. 2009, *ApJ*, 705, L128
- Rugel, G., Faestermann, T., Knie, K., et al. 2009, *Phys. Rev. Lett.*, 103, 072502
- Ruiter, A. J., Belczynski, K., Sim, S. A., et al. 2011, *MNRAS*, 417, 408
- Ruiter, A. J., Belczynski, K., Sim, S. A., Seitenzahl, I. R., & Kwiatkowski, D. 2014, *MNRAS*, 440, L101
- Saio, H. & Nomoto, K. 1985, *A&A*, 150, L21
- Schwab, J., Martínez-Rodríguez, H., Piro, A. L., & Badenes, C. 2017, *ApJ*, 851, 105
- Seitenzahl, I. R., Ciaraldi-Schoolmann, F., Röpke, F. K., et al. 2013, *MNRAS*, 429, 1156
- Seitenzahl, I. R., Kromer, M., Ohlmann, S. T., et al. 2016, *A&A*, 592, A57
- Seitenzahl, I. R., Timmes, F. X., Marin-Lafèche, A., et al. 2008, *ApJ*, 685, L129
- Sharon, A. & Kushnir, D. 2020, *Research Notes of the American Astronomical Society*, 4, 158
- Shen, K. J., Bildsten, L., Kasen, D., & Quataert, E. 2012, *ApJ*, 748, 35
- Shen, K. J., Blondin, S., Kasen, D., et al. 2021, *ApJ*, 909, L18
- Shen, K. J., Kasen, D., Miles, B. J., & Townsley, D. M. 2018, *ApJ*, 854, 52
- Shen, K. J. & Moore, K. 2014, *ApJ*, 797, 46
- Sigurdsson, S. & Phinney, E. S. 1993, *ApJ*, 415, 631
- Sim, S. A., Röpke, F. K., Hillebrandt, W., et al. 2010, *ApJ*, 714, L52
- Soker, N. 2019, *New A Rev.*, 87, 101535
- Timmes, F. X., Brown, E. F., & Truran, J. W. 2003, *ApJ*, 590, L83
- Timmes, F. X., Woosley, S. E., & Taam, R. E. 1994, *ApJ*, 420, 348
- Toonen, S., Perets, H. B., & Hamers, A. S. 2018, *A&A*, 610, A22
- Townsley, D. M., Miles, B. J., Shen, K. J., & Kasen, D. 2019, *ApJ*, 878, L38
- Turcotte, S. & Wimmer-Schweingruber, R. F. 2002, *Journal of Geophysical Research (Space Physics)*, 107, 1442
- Wang, B. 2018, *Research in Astronomy and Astrophysics*, 18, 049
- Wang, C.-Y. 2005, *ApJ*, 626, 183
- Webbink, R. F. 1984, *ApJ*, 277, 355
- Wilk, K. D., Hillier, D. J., & Dessart, L. 2018, *MNRAS*, 474, 3187
- Wilk, K. D., Hillier, D. J., & Dessart, L. 2020, *MNRAS*, 494, 2221
- Woosley, S. E., Arnett, W. D., & Clayton, D. D. 1973, *ApJS*, 26, 231
- Woosley, S. E., Kasen, D., Blinnikov, S., & Sorokina, E. 2007, *ApJ*, 662, 487
- Zhou, Y. 2017, *Phys. Rep.*, 723, 1

List of Objects

‘SN 2017bzc’ on page 12

Appendix A: Basic model properties and nickel isotopic abundances

Table A.1 gives basic properties and nickel isotopic abundances of the models discussed in Sect. 3.5 (see also Fig. 5). Column headings are described hereafter:

- (1) model name
- (2) dimension of the numerical simulation (1D, 2D, or 3D)
- (3) total progenitor mass. We include the helium-shell mass for sub- M_{Ch} double-detonation models, whereas for the violent WD merger and WD-WD collision models, we give the total ejecta mass (equal to the combined mass of the two WDs)
- (4) composition of the progenitor WD star prior to thermonuclear runaway. We only report the mass fractions of ^{12}C , ^{16}O , and ^{22}Ne for the CO core (i.e. excluding the He shell for double-detonation models). The ^{22}Ne mass fraction is almost always adjusted by hand to mimic a given metallicity, but the exact value assumed for a solar-metallicity WD ($X(^{22}\text{Ne}) \approx 0.013$ according to Eq. 1) varies among different authors between 0.01 and 0.025. One exception is the M_{Ch} delayed-detonation model 5p0_Z0p014 published here for the first time. The ^{22}Ne abundance (and C/O ratio) in this model results from a stellar-evolution calculation and takes into account the convective burning (or ‘simmering’) phase prior to thermonuclear runaway as in Bravo et al. (2010)
- (5) radioactive ^{56}Ni yield shortly after explosion ($t \approx 0$)
- (6) decayed stable ^{58}Ni yield at $t = 1$ yr past explosion. The ^{58}Ni yield at $t = 1$ yr is essentially the same as at $t \approx 0$ (see Sect. 3.5)
- (7) total decayed stable Ni yield (including all stable isotopes: ^{58}Ni , ^{60}Ni , ^{61}Ni , ^{62}Ni , and ^{64}Ni) at $t = 1$ yr past explosion. Since ^{58}Ni is the only stable Ni isotope in the WD-WD collision models of Kushnir (2021, private communication), the total stable Ni yield is the same as the ^{58}Ni yield
- (8) main reference for the model

Table A.1. Basic model properties and nickel isotopic abundances.

Model	Dimension	M_{tot} (M_{\odot})	X_{init} $^{12}\text{C} / ^{16}\text{O} / ^{22}\text{Ne}$	$M(^{56}\text{Ni})_{t=0}$ (M_{\odot})	$M(^{58}\text{Ni})_{t=1 \text{ yr}}$ (M_{\odot})	$M(\text{Ni}_{\text{stable}})_{t=1 \text{ yr}}$ (M_{\odot})	Reference
(1)	(2)	(3)	(4)	(5)	(6)	(7)	(8)
<i>M_{Ch} Deflagrations</i>							
N1def	3D	1.40	0.475 / 0.500 / 2.5(−2)	0.063	7.41 (−3)	7.78 (−3)	Fink et al. (2014)
N3def	3D	1.40	0.475 / 0.500 / 2.5(−2)	0.084	1.31 (−2)	1.40 (−2)	Fink et al. (2014)
N5def	3D	1.40	0.475 / 0.500 / 2.5(−2)	0.174	2.39 (−2)	2.52 (−2)	Fink et al. (2014)
N10def	3D	1.40	0.475 / 0.500 / 2.5(−2)	0.197	3.00 (−2)	3.17 (−2)	Fink et al. (2014)
N20def	3D	1.40	0.475 / 0.500 / 2.5(−2)	0.266	4.20 (−2)	4.48 (−2)	Fink et al. (2014)
N40def	3D	1.40	0.475 / 0.500 / 2.5(−2)	0.335	5.54 (−2)	5.89 (−2)	Fink et al. (2014)
N100def	3D	1.40	0.475 / 0.500 / 2.5(−2)	0.360	6.07 (−2)	6.48 (−2)	Fink et al. (2014)
N100Hdef	3D	1.42	0.475 / 0.500 / 2.5(−2)	0.333	5.93 (−2)	6.94 (−2)	Fink et al. (2014)
N100Ldef	3D	1.36	0.475 / 0.500 / 2.5(−2)	0.330	3.23 (−2)	3.29 (−2)	Fink et al. (2014)
N150def	3D	1.40	0.475 / 0.500 / 2.5(−2)	0.385	6.53 (−2)	6.97 (−2)	Fink et al. (2014)
N300Cdef	3D	1.40	0.475 / 0.500 / 2.5(−2)	0.340	5.92 (−2)	6.39 (−2)	Fink et al. (2014)
N200def	3D	1.40	0.475 / 0.500 / 2.5(−2)	0.379	7.20 (−2)	7.68 (−2)	Fink et al. (2014)
N1600def	3D	1.40	0.475 / 0.500 / 2.5(−2)	0.347	7.39 (−2)	7.98 (−2)	Fink et al. (2014)
N1600Cdef	3D	1.40	0.475 / 0.500 / 2.5(−2)	0.320	6.12 (−2)	6.80 (−2)	Fink et al. (2014)
W7	1D	1.38	0.475 / 0.500 / 2.5(−2)	0.651	6.94 (−2)	7.46 (−2)	Mori et al. (2018)
W7_Z0.1	1D	1.38	0.498 / 0.500 / 2.5(−3)	0.645	5.95 (−2)	6.31 (−2)	Leung & Nomoto (2018)
W7_Z0.5	1D	1.38	0.488 / 0.500 / 1.3(−2)	0.651	5.98 (−2)	6.34 (−2)	Leung & Nomoto (2018)
W7_Zsun	1D	1.38	0.475 / 0.500 / 2.5(−2)	0.659	6.20 (−2)	6.56 (−2)	Leung & Nomoto (2018)
<i>M_{Ch} Delayed Detonations</i>							
N1	3D	1.40	0.475 / 0.500 / 2.5(−2)	1.110	7.26 (−2)	7.53 (−2)	Seitenzahl et al. (2013)
N3	3D	1.40	0.475 / 0.500 / 2.5(−2)	1.040	6.78 (−2)	7.13 (−2)	Seitenzahl et al. (2013)
N5	3D	1.40	0.475 / 0.500 / 2.5(−2)	0.974	6.98 (−2)	7.39 (−2)	Seitenzahl et al. (2013)
N10	3D	1.40	0.475 / 0.500 / 2.5(−2)	0.939	7.13 (−2)	7.58 (−2)	Seitenzahl et al. (2013)
N20	3D	1.40	0.475 / 0.500 / 2.5(−2)	0.778	6.63 (−2)	7.15 (−2)	Seitenzahl et al. (2013)
N40	3D	1.40	0.475 / 0.500 / 2.5(−2)	0.655	6.89 (−2)	7.39 (−2)	Seitenzahl et al. (2013)
N100	3D	1.40	0.475 / 0.500 / 2.5(−2)	0.604	6.90 (−2)	7.40 (−2)	Seitenzahl et al. (2013)
N100H	3D	1.42	0.475 / 0.500 / 2.5(−2)	0.694	7.54 (−2)	8.72 (−2)	Seitenzahl et al. (2013)
N100L	3D	1.36	0.475 / 0.500 / 2.5(−2)	0.532	3.81 (−2)	3.91 (−2)	Seitenzahl et al. (2013)
N100_Z0.01	3D	1.40	0.500 / 0.500 / 2.5(−4)	0.655	5.01 (−2)	5.56 (−2)	Seitenzahl et al. (2013)
N100_Z0.1	3D	1.40	0.498 / 0.500 / 2.5(−3)	0.649	5.09 (−2)	5.65 (−2)	Seitenzahl et al. (2013)
N100_Z0.5	3D	1.40	0.488 / 0.500 / 1.3(−2)	0.629	5.90 (−2)	6.42 (−2)	Seitenzahl et al. (2013)
N150	3D	1.40	0.475 / 0.500 / 2.5(−2)	0.566	7.01 (−2)	7.50 (−2)	Seitenzahl et al. (2013)
N200	3D	1.40	0.475 / 0.500 / 2.5(−2)	0.415	7.29 (−2)	7.77 (−2)	Seitenzahl et al. (2013)
N300C	3D	1.40	0.475 / 0.500 / 2.5(−2)	0.512	6.26 (−2)	6.75 (−2)	Seitenzahl et al. (2013)
N1600	3D	1.40	0.475 / 0.500 / 2.5(−2)	0.364	7.48 (−2)	8.07 (−2)	Seitenzahl et al. (2013)
N1600C	3D	1.40	0.475 / 0.500 / 2.5(−2)	0.322	6.16 (−2)	6.85 (−2)	Seitenzahl et al. (2013)
M1.33_zscl_z0	2D	1.33	0.500 / 0.500 / 0.0	0.782	2.13 (−2)	3.23 (−2)	Kobayashi et al. (2020)
M1.33_zscl_z0p002	2D	1.33	0.499 / 0.499 / ... ^a	0.781	2.16 (−2)	3.26 (−2)	Kobayashi et al. (2020)
M1.33_zscl_z0p01	2D	1.33	0.495 / 0.495 / ... ^a	0.778	2.18 (−2)	3.30 (−2)	Kobayashi et al. (2020)
M1.33_zscl_z0p02	2D	1.33	0.490 / 0.490 / ... ^a	0.775	2.24 (−2)	3.38 (−2)	Kobayashi et al. (2020)
M1.33_zscl_z0p04	2D	1.33	0.480 / 0.480 / ... ^a	0.770	2.37 (−2)	3.57 (−2)	Kobayashi et al. (2020)
M1.37_zscl_z0	2D	1.37	0.500 / 0.500 / 0.0	0.680	4.29 (−2)	5.58 (−2)	Kobayashi et al. (2020)
M1.37_zscl_z0p002	2D	1.37	0.499 / 0.499 / ... ^a	0.678	4.32 (−2)	5.61 (−2)	Kobayashi et al. (2020)
M1.37_zscl_z0p01	2D	1.37	0.495 / 0.495 / ... ^a	0.675	4.36 (−2)	5.66 (−2)	Kobayashi et al. (2020)
M1.37_zscl_z0p02	2D	1.37	0.490 / 0.490 / ... ^a	0.673	4.42 (−2)	5.74 (−2)	Kobayashi et al. (2020)
M1.37_zscl_z0p04	2D	1.37	0.480 / 0.480 / ... ^a	0.669	4.51 (−2)	5.88 (−2)	Kobayashi et al. (2020)
M1.38_zscl_z0	2D	1.38	0.500 / 0.500 / 0.0	0.649	4.83 (−2)	6.70 (−2)	Kobayashi et al. (2020)
M1.38_zscl_z0p002	2D	1.38	0.499 / 0.499 / ... ^a	0.647	4.85 (−2)	6.73 (−2)	Kobayashi et al. (2020)
M1.38_zscl_z0p01	2D	1.38	0.495 / 0.495 / ... ^a	0.644	4.89 (−2)	6.77 (−2)	Kobayashi et al. (2020)
M1.38_zscl_z0p02	2D	1.38	0.490 / 0.490 / ... ^a	0.642	4.94 (−2)	6.84 (−2)	Kobayashi et al. (2020)
M1.38_zscl_z0p04	2D	1.38	0.480 / 0.480 / ... ^a	0.638	5.04 (−2)	6.98 (−2)	Kobayashi et al. (2020)
M1.33_zne22_z0	2D	1.33	0.500 / 0.500 / 0.0	0.845	2.13 (−2)	3.23 (−2)	Kobayashi et al. (2020)
M1.33_zne22_z0p002	2D	1.33	0.499 / 0.499 / 2.0 (−3)	0.838	2.19 (−2)	3.33 (−2)	Kobayashi et al. (2020)
M1.33_zne22_z0p01	2D	1.33	0.495 / 0.495 / 1.0 (−2)	0.750	3.15 (−2)	4.34 (−2)	Kobayashi et al. (2020)
M1.33_zne22_z0p02	2D	1.33	0.490 / 0.490 / 2.0 (−2)	0.724	4.60 (−2)	5.79 (−2)	Kobayashi et al. (2020)
M1.33_zne22_z0p04	2D	1.33	0.480 / 0.480 / 4.0 (−2)	0.678	7.49 (−2)	8.70 (−2)	Kobayashi et al. (2020)
M1.37_zne22_z0	2D	1.37	0.500 / 0.500 / 0.0	0.696	4.29 (−2)	5.58 (−2)	Kobayashi et al. (2020)
M1.37_zne22_z0p002	2D	1.37	0.499 / 0.499 / 2.0 (−3)	0.689	4.37 (−2)	5.69 (−2)	Kobayashi et al. (2020)
M1.37_zne22_z0p01	2D	1.37	0.495 / 0.495 / 1.0 (−2)	0.650	5.17 (−2)	6.52 (−2)	Kobayashi et al. (2020)
M1.37_zne22_z0p02	2D	1.37	0.490 / 0.490 / 2.0 (−2)	0.627	6.36 (−2)	7.71 (−2)	Kobayashi et al. (2020)
M1.37_zne22_z0p04	2D	1.37	0.480 / 0.480 / 4.0 (−2)	0.587	8.70 (−2)	1.00 (−1)	Kobayashi et al. (2020)
M1.38_zne22_z0	2D	1.38	0.500 / 0.500 / 0.0	0.675	4.83 (−2)	6.70 (−2)	Kobayashi et al. (2020)
M1.38_zne22_z0p002	2D	1.38	0.499 / 0.499 / 2.0 (−3)	0.669	4.90 (−2)	6.80 (−2)	Kobayashi et al. (2020)
M1.38_zne22_z0p01	2D	1.38	0.495 / 0.495 / 1.0 (−2)	0.620	5.65 (−2)	7.58 (−2)	Kobayashi et al. (2020)

Table A.1. continued.

Model	Dimension	M_{tot} (M_{\odot})	X_{init} $^{12}\text{C} / ^{16}\text{O} / ^{22}\text{Ne}$	$M(^{56}\text{Ni})_{t=0}$ (M_{\odot})	$M(^{58}\text{Ni})_{t=1 \text{ yr}}$ (M_{\odot})	$M(\text{Ni}_{\text{stable}})_{t=1 \text{ yr}}$ (M_{\odot})	Reference
(1)	(2)	(3)	(4)	(5)	(6)	(7)	(8)
M1.38_zne22_z0p02	2D	1.38	0.490 / 0.490 / 2.0 (–2)	0.598	6.77 (–2)	8.70 (–2)	Kobayashi et al. (2020)
M1.38_zne22_z0p04	2D	1.38	0.480 / 0.480 / 4.0 (–2)	0.560	8.98 (–2)	1.09 (–1)	Kobayashi et al. (2020)
DDC0	1D	1.41	0.491 / 0.491 / 1.4 (–2)	0.840	3.52 (–2)	4.69 (–2)	Blondin et al. (2013)
DDC6	1D	1.41	0.491 / 0.491 / 1.4 (–2)	0.709	2.63 (–2)	3.04 (–2)	Blondin et al. (2013)
DDC10	1D	1.41	0.491 / 0.491 / 1.4 (–2)	0.614	2.58 (–2)	2.99 (–2)	Blondin et al. (2013)
DDC15	1D	1.41	0.491 / 0.491 / 1.4 (–2)	0.507	2.56 (–2)	2.97 (–2)	Blondin et al. (2013)
DDC17	1D	1.41	0.491 / 0.491 / 1.4 (–2)	0.407	2.53 (–2)	2.94 (–2)	Blondin et al. (2013)
DDC20	1D	1.41	0.491 / 0.491 / 1.4 (–2)	0.297	2.51 (–2)	2.92 (–2)	Blondin et al. (2013)
DDC22	1D	1.41	0.491 / 0.491 / 1.4 (–2)	0.201	2.48 (–2)	2.89 (–2)	Blondin et al. (2013)
DDC25	1D	1.41	0.491 / 0.491 / 1.4 (–2)	0.125	2.43 (–2)	2.85 (–2)	Blondin et al. (2013)
5p0_Z0p014	1D	1.37	0.460 / 0.506 / 2.7 (–2)	0.601	3.14 (–2)	3.87 (–2)	This paper
<i>M_{Ch} Gravitationally-Confined Detonations</i>							
GCD200	3D	1.40	0.475 / 0.500 / 2.5 (–2)	0.742	3.74 (–2)	3.95 (–2)	Seitenzahl et al. (2016)
<i>$\text{Sub-}M_{\text{Ch}}$ Detonations</i>							
SCH1p5	1D	0.88	0.491 / 0.491 / 1.4 (–2)	0.080	1.21 (–3)	1.48 (–3)	Blondin et al. (2017)
SCH2p0	1D	0.90	0.491 / 0.491 / 1.4 (–2)	0.118	1.37 (–3)	1.64 (–3)	Blondin et al. (2017)
SCH2p5	1D	0.93	0.491 / 0.491 / 1.4 (–2)	0.172	1.55 (–3)	1.79 (–3)	Blondin et al. (2017)
SCH3p0	1D	0.95	0.491 / 0.491 / 1.4 (–2)	0.233	1.74 (–3)	1.96 (–3)	Blondin et al. (2017)
SCH3p5	1D	0.98	0.491 / 0.491 / 1.4 (–2)	0.306	1.97 (–3)	2.17 (–3)	Blondin et al. (2017)
SCH4p0	1D	1.00	0.491 / 0.491 / 1.4 (–2)	0.386	2.42 (–3)	2.63 (–3)	Blondin et al. (2017)
SCH4p5	1D	1.03	0.491 / 0.491 / 1.4 (–2)	0.470	5.66 (–3)	7.33 (–3)	Blondin et al. (2017)
SCH5p0	1D	1.05	0.491 / 0.491 / 1.4 (–2)	0.554	8.58 (–3)	1.23 (–2)	Blondin et al. (2017)
SCH5p5	1D	1.08	0.491 / 0.491 / 1.4 (–2)	0.637	1.17 (–2)	1.66 (–2)	Blondin et al. (2017)
SCH6p0	1D	1.10	0.491 / 0.491 / 1.4 (–2)	0.712	1.50 (–2)	2.09 (–2)	Blondin et al. (2017)
SCH6p5	1D	1.13	0.491 / 0.491 / 1.4 (–2)	0.778	2.09 (–2)	2.74 (–2)	Blondin et al. (2017)
SCH7p0	1D	1.15	0.491 / 0.491 / 1.4 (–2)	0.842	2.60 (–2)	3.30 (–2)	Blondin et al. (2017)
1.00_5050_xsun	1D	1.00	0.493 / 0.493 / 1.0 (–2)	0.554	7.05 (–3)	1.71 (–2)	Shen et al. (2018)
1.00_5050_z0p0	1D	1.00	0.500 / 0.500 / 0.0	0.580	1.06 (–3)	1.05 (–2)	Shen et al. (2018)
1.00_5050_z0p5	1D	1.00	0.497 / 0.497 / 5.0 (–3)	0.566	2.48 (–3)	1.24 (–2)	Shen et al. (2018)
1.00_5050_z2p0	1D	1.00	0.487 / 0.487 / 2.0 (–2)	0.533	1.66 (–2)	2.74 (–2)	Shen et al. (2018)
1p06_Z2p25e-2	1D	1.06	0.476 / 0.498 / 2.2 (–2)	0.657	2.41 (–2)	3.16 (–2)	Bravo et al. (2019)
0p88_Z2p25e-2	1D	0.88	0.476 / 0.498 / 2.2 (–2)	0.167	2.86 (–3)	3.20 (–3)	Bravo et al. (2019)
det_0.81	1D	0.82	0.500 / 0.500 / 0.0	0.009	1.62 (–5)	1.63 (–5)	Sim et al. (2010)
det_0.88	1D	0.89	0.500 / 0.500 / 0.0	0.070	2.59 (–5)	2.62 (–5)	Sim et al. (2010)
det_0.97	1D	0.98	0.500 / 0.500 / 0.0	0.301	5.70 (–5)	7.18 (–5)	Sim et al. (2010)
det_1.06	1D	1.06	0.500 / 0.500 / 0.0	0.559	9.03 (–4)	3.08 (–3)	Sim et al. (2010)
det_1.06_0.075Ne	1D	1.06	0.425 / 0.500 / 7.5 (–2)	0.434	5.22 (–2)	5.23 (–2)	Sim et al. (2010)
det_1.15	1D	1.15	0.500 / 0.500 / 0.0	0.809	1.75 (–3)	5.99 (–3)	Sim et al. (2010)
CIWD_13	1D	0.80	0.500 / 0.500 / 0.0	0.055	2.22 (–5)	2.35 (–5)	Kushnir et al. (2020)
CIWD_324w	1D	0.80	0.500 / 0.500 / 0.0	0.053	2.61 (–5)	2.70 (–5)	Kushnir et al. (2020)
CIWD_157	1D	0.80	0.496 / 0.496 / 7.5 (–3)	0.036	4.87 (–4)	4.87 (–4)	Kushnir et al. (2020)
CIWD_416	1D	0.80	0.491 / 0.491 / 1.4 (–2)	0.026	9.42 (–4)	1.24 (–3)	Kushnir et al. (2020)
CIWD_415	1D	0.80	0.492 / 0.492 / 1.4 (–2)	0.026	9.38 (–4)	1.18 (–3)	Kushnir et al. (2020)
CIWD_174	1D	0.80	0.492 / 0.492 / 1.5 (–2)	0.027	9.39 (–4)	9.41 (–4)	Kushnir et al. (2020)
CIWD_364w	1D	0.80	0.492 / 0.492 / 1.5 (–2)	0.026	9.32 (–4)	9.34 (–4)	Kushnir et al. (2020)
CIWD_438	1D	0.80	0.693 / 0.292 / 1.5 (–2)	0.049	1.06 (–3)	1.07 (–3)	Kushnir et al. (2020)
CIWD_433	1D	0.80	0.292 / 0.693 / 1.5 (–2)	0.015	5.71 (–4)	5.71 (–4)	Kushnir et al. (2020)
CIWD_318	1D	0.80	0.485 / 0.485 / 3.0 (–2)	0.018	1.75 (–3)	1.76 (–3)	Kushnir et al. (2020)
CIWD_49	1D	0.85	0.500 / 0.500 / 0.0	0.144	2.46 (–5)	2.63 (–5)	Kushnir et al. (2020)
CIWD_332w	1D	0.85	0.500 / 0.500 / 0.0	0.138	2.76 (–5)	2.86 (–5)	Kushnir et al. (2020)
CIWD_158	1D	0.85	0.496 / 0.496 / 7.5 (–3)	0.129	6.55 (–4)	6.56 (–4)	Kushnir et al. (2020)
CIWD_420	1D	0.85	0.491 / 0.491 / 1.4 (–2)	0.110	1.33 (–3)	1.54 (–3)	Kushnir et al. (2020)
CIWD_419	1D	0.85	0.492 / 0.492 / 1.4 (–2)	0.113	1.33 (–3)	1.50 (–3)	Kushnir et al. (2020)
CIWD_210	1D	0.85	0.492 / 0.492 / 1.5 (–2)	0.121	1.34 (–3)	1.34 (–3)	Kushnir et al. (2020)
CIWD_372w	1D	0.85	0.492 / 0.492 / 1.5 (–2)	0.114	1.33 (–3)	1.33 (–3)	Kushnir et al. (2020)
CIWD_439	1D	0.85	0.693 / 0.292 / 1.5 (–2)	0.169	1.48 (–3)	1.48 (–3)	Kushnir et al. (2020)
CIWD_434	1D	0.85	0.292 / 0.693 / 1.5 (–2)	0.048	8.65 (–4)	8.66 (–4)	Kushnir et al. (2020)
CIWD_319	1D	0.85	0.485 / 0.485 / 3.0 (–2)	0.114	2.68 (–3)	2.69 (–3)	Kushnir et al. (2020)
CIWD_82	1D	0.90	0.500 / 0.500 / 0.0	0.284	3.35 (–5)	3.56 (–5)	Kushnir et al. (2020)
CIWD_340w	1D	0.90	0.500 / 0.500 / 0.0	0.276	2.96 (–5)	3.12 (–5)	Kushnir et al. (2020)
CIWD_159	1D	0.90	0.496 / 0.496 / 7.5 (–3)	0.267	8.50 (–4)	8.50 (–4)	Kushnir et al. (2020)
CIWD_424	1D	0.90	0.491 / 0.491 / 1.4 (–2)	0.249	1.78 (–3)	1.93 (–3)	Kushnir et al. (2020)
CIWD_423	1D	0.90	0.492 / 0.492 / 1.4 (–2)	0.251	1.77 (–3)	1.89 (–3)	Kushnir et al. (2020)
CIWD_435	1D	0.90	0.292 / 0.693 / 1.5 (–2)	0.193	1.53 (–3)	1.53 (–3)	Kushnir et al. (2020)
CIWD_440	1D	0.90	0.693 / 0.292 / 1.5 (–2)	0.306	2.00 (–3)	2.00 (–3)	Kushnir et al. (2020)

Table A.1. continued.

Model	Dimension	M_{tot} (M_{\odot})	X_{init} $^{12}\text{C} / ^{16}\text{O} / ^{22}\text{Ne}$	$M(^{56}\text{Ni})_{t=0}$ (M_{\odot})	$M(^{58}\text{Ni})_{t=1 \text{ yr}}$ (M_{\odot})	$M(\text{Ni}_{\text{stable}})_{t=1 \text{ yr}}$ (M_{\odot})	Reference
(1)	(2)	(3)	(4)	(5)	(6)	(7)	(8)
CIWD_243	1D	0.90	0.492 / 0.492 / 1.5 (−2)	0.259	1.80 (−3)	1.80 (−3)	Kushnir et al. (2020)
CIWD_380w	1D	0.90	0.492 / 0.492 / 1.5 (−2)	0.251	1.78 (−3)	1.79 (−3)	Kushnir et al. (2020)
CIWD_320	1D	0.90	0.485 / 0.485 / 3.0 (−2)	0.250	3.78 (−3)	3.79 (−3)	Kushnir et al. (2020)
CIWD_113	1D	1.00	0.500 / 0.500 / 0.0	0.570	3.11 (−3)	6.56 (−3)	Kushnir et al. (2020)
CIWD_348w	1D	1.00	0.500 / 0.500 / 0.0	0.564	1.40 (−3)	2.27 (−3)	Kushnir et al. (2020)
CIWD_160	1D	1.00	0.496 / 0.496 / 7.5 (−3)	0.552	3.20 (−3)	7.11 (−3)	Kushnir et al. (2020)
CIWD_428	1D	1.00	0.491 / 0.491 / 1.4 (−2)	0.532	7.09 (−3)	8.41 (−3)	Kushnir et al. (2020)
CIWD_427	1D	1.00	0.492 / 0.492 / 1.4 (−2)	0.533	7.10 (−3)	8.47 (−3)	Kushnir et al. (2020)
CIWD_441	1D	1.00	0.693 / 0.292 / 1.5 (−2)	0.573	9.98 (−3)	1.60 (−2)	Kushnir et al. (2020)
CIWD_274	1D	1.00	0.492 / 0.492 / 1.5 (−2)	0.539	8.47 (−3)	1.25 (−2)	Kushnir et al. (2020)
CIWD_388w	1D	1.00	0.492 / 0.492 / 1.5 (−2)	0.533	7.25 (−3)	8.55 (−3)	Kushnir et al. (2020)
CIWD_436	1D	1.00	0.292 / 0.693 / 1.5 (−2)	0.498	6.68 (−3)	8.64 (−3)	Kushnir et al. (2020)
CIWD_321	1D	1.00	0.485 / 0.485 / 3.0 (−2)	0.519	2.01 (−2)	2.46 (−2)	Kushnir et al. (2020)
CIWD_140	1D	1.10	0.500 / 0.500 / 0.0	0.827	8.16 (−3)	1.78 (−2)	Kushnir et al. (2020)
CIWD_356w	1D	1.10	0.500 / 0.500 / 0.0	0.825	6.88 (−3)	1.62 (−2)	Kushnir et al. (2020)
CIWD_161	1D	1.10	0.496 / 0.496 / 7.5 (−3)	0.809	6.10 (−3)	1.66 (−2)	Kushnir et al. (2020)
CIWD_432	1D	1.10	0.491 / 0.491 / 1.4 (−2)	0.790	1.69 (−2)	2.67 (−2)	Kushnir et al. (2020)
CIWD_431	1D	1.10	0.492 / 0.492 / 1.4 (−2)	0.791	1.68 (−2)	2.66 (−2)	Kushnir et al. (2020)
CIWD_301	1D	1.10	0.492 / 0.492 / 1.5 (−2)	0.792	1.71 (−2)	2.75 (−2)	Kushnir et al. (2020)
CIWD_396w	1D	1.10	0.492 / 0.492 / 1.5 (−2)	0.791	1.73 (−2)	2.71 (−2)	Kushnir et al. (2020)
CIWD_442	1D	1.10	0.693 / 0.292 / 1.5 (−2)	0.812	1.81 (−2)	3.02 (−2)	Kushnir et al. (2020)
CIWD_437	1D	1.10	0.292 / 0.693 / 1.5 (−2)	0.769	1.61 (−2)	2.46 (−2)	Kushnir et al. (2020)
CIWD_322	1D	1.10	0.485 / 0.485 / 3.0 (−2)	0.762	4.07 (−2)	5.10 (−2)	Kushnir et al. (2020)
ddet_M1a	3D	1.05	0.500 / 0.500 / 0.0	0.574	1.23 (−3)	1.71 (−2)	Gronow et al. (2020)
ddet_M2a	3D	1.05	0.500 / 0.500 / 0.0	0.587	1.15 (−3)	1.41 (−2)	Gronow et al. (2020)
ddet_M2a_13	3D	1.05	0.500 / 0.500 / 0.0	0.439	1.71 (−3)	1.68 (−2)	Gronow et al. (2020)
ddet_M2a_21	3D	1.05	0.500 / 0.500 / 0.0	0.572	1.11 (−3)	1.59 (−2)	Gronow et al. (2020)
ddet_M2a_36	3D	1.05	0.500 / 0.500 / 0.0	0.571	1.08 (−3)	1.60 (−2)	Gronow et al. (2020)
ddet_M2a_79	3D	1.05	0.500 / 0.500 / 0.0	0.576	1.04 (−3)	1.47 (−2)	Gronow et al. (2020)
ddet_M2a_i55	3D	1.05	0.500 / 0.500 / 0.0	0.601	1.18 (−3)	1.49 (−2)	Gronow et al. (2020)
ddet_M2b	3D	1.05	0.500 / 0.500 / 0.0	0.588	1.15 (−3)	1.40 (−2)	Gronow et al. (2020)
ddet_M3a	3D	0.91	0.500 / 0.500 / 0.0	0.337	1.15 (−3)	8.18 (−3)	Gronow et al. (2020)
ddet_M08_03	3D	0.83	0.500 / 0.490 / 1.0 (−2)	0.132	2.03 (−3)	2.25 (−3)	Gronow et al. (2021)
ddet_M08_05	3D	0.86	0.500 / 0.490 / 1.0 (−2)	0.201	3.27 (−3)	3.64 (−3)	Gronow et al. (2021)
ddet_M08_10	3D	0.91	0.500 / 0.490 / 1.0 (−2)	0.312	1.05 (−2)	1.50 (−2)	Gronow et al. (2021)
ddet_M08_10_r	3D	0.91	0.500 / 0.490 / 1.0 (−2)	0.327	8.06 (−3)	1.29 (−2)	Gronow et al. (2021)
ddet_M09_03	3D	0.93	0.500 / 0.490 / 1.0 (−2)	0.330	7.01 (−3)	8.34 (−3)	Gronow et al. (2021)
ddet_M09_05	3D	0.95	0.500 / 0.490 / 1.0 (−2)	0.386	1.05 (−2)	1.46 (−2)	Gronow et al. (2021)
ddet_M09_10	3D	1.00	0.500 / 0.490 / 1.0 (−2)	0.487	1.81 (−2)	2.63 (−2)	Gronow et al. (2021)
ddet_M09_10_r	3D	1.00	0.500 / 0.490 / 1.0 (−2)	0.503	1.62 (−2)	2.73 (−2)	Gronow et al. (2021)
ddet_M10_02	3D	1.03	0.500 / 0.490 / 1.0 (−2)	0.541	1.70 (−2)	2.55 (−2)	Gronow et al. (2021)
ddet_M10_03	3D	1.06	0.500 / 0.490 / 1.0 (−2)	0.591	2.05 (−2)	3.15 (−2)	Gronow et al. (2021)
ddet_M10_05	3D	1.06	0.500 / 0.490 / 1.0 (−2)	0.547	1.84 (−2)	3.04 (−2)	Gronow et al. (2021)
ddet_M10_10	3D	1.11	0.500 / 0.490 / 1.0 (−2)	0.762	2.61 (−2)	4.26 (−2)	Gronow et al. (2021)
ddet_M11_05	3D	1.16	0.500 / 0.490 / 1.0 (−2)	0.838	3.06 (−2)	4.95 (−2)	Gronow et al. (2021)
M0.90_zscl_z0	2D	0.95	0.500 / 0.500 / 0.0	0.029	6.86 (−5)	6.49 (−4)	Kobayashi et al. (2020)
M0.90_zscl_z0p002	2D	0.95	0.499 / 0.499 / ... ^a	0.028	2.11 (−4)	8.34 (−4)	Kobayashi et al. (2020)
M0.90_zscl_z0p01	2D	0.95	0.495 / 0.495 / ... ^a	0.027	4.27 (−4)	1.12 (−3)	Kobayashi et al. (2020)
M0.90_zscl_z0p02	2D	0.95	0.490 / 0.490 / ... ^a	0.025	5.98 (−4)	1.45 (−3)	Kobayashi et al. (2020)
M0.90_zscl_z0p04	2D	0.95	0.480 / 0.480 / ... ^a	0.023	8.89 (−4)	2.03 (−3)	Kobayashi et al. (2020)
M1.00_zscl_z0	2D	1.05	0.500 / 0.500 / 0.0	0.643	9.63 (−4)	8.98 (−3)	Kobayashi et al. (2020)
M1.00_zscl_z0p002	2D	1.05	0.499 / 0.499 / ... ^a	0.642	1.06 (−3)	9.14 (−3)	Kobayashi et al. (2020)
M1.00_zscl_z0p01	2D	1.05	0.495 / 0.495 / ... ^a	0.641	1.08 (−3)	9.41 (−3)	Kobayashi et al. (2020)
M1.00_zscl_z0p02	2D	1.05	0.490 / 0.490 / ... ^a	0.639	1.34 (−3)	1.00 (−2)	Kobayashi et al. (2020)
M1.00_zscl_z0p04	2D	1.05	0.480 / 0.480 / ... ^a	0.635	3.00 (−3)	1.20 (−2)	Kobayashi et al. (2020)
M1.10_zscl_z0	2D	1.15	0.500 / 0.500 / 0.0	0.861	1.13 (−3)	1.13 (−2)	Kobayashi et al. (2020)
M1.10_zscl_z0p002	2D	1.15	0.499 / 0.499 / ... ^a	0.860	1.47 (−3)	1.17 (−2)	Kobayashi et al. (2020)
M1.10_zscl_z0p01	2D	1.15	0.495 / 0.495 / ... ^a	0.859	1.60 (−3)	1.21 (−2)	Kobayashi et al. (2020)
M1.10_zscl_z0p02	2D	1.15	0.490 / 0.490 / ... ^a	0.857	2.39 (−3)	1.32 (−2)	Kobayashi et al. (2020)
M1.10_zscl_z0p04	2D	1.15	0.480 / 0.480 / ... ^a	0.853	4.60 (−3)	1.57 (−2)	Kobayashi et al. (2020)
M1.20_zscl_z0	2D	1.25	0.500 / 0.500 / 0.0	1.052	5.16 (−3)	1.55 (−2)	Kobayashi et al. (2020)
M1.20_zscl_z0p002	2D	1.25	0.499 / 0.499 / ... ^a	1.052	5.64 (−3)	1.60 (−2)	Kobayashi et al. (2020)
M1.20_zscl_z0p01	2D	1.25	0.495 / 0.495 / ... ^a	1.050	6.51 (−3)	1.70 (−2)	Kobayashi et al. (2020)
M1.20_zscl_z0p02	2D	1.25	0.490 / 0.490 / ... ^a	1.049	7.32 (−3)	1.80 (−2)	Kobayashi et al. (2020)
M1.20_zscl_z0p04	2D	1.25	0.480 / 0.480 / ... ^a	1.043	1.06 (−2)	2.15 (−2)	Kobayashi et al. (2020)

Table A.1. continued.

Model	Dimension	M_{tot} (M_{\odot})	X_{init} $^{12}\text{C} / ^{16}\text{O} / ^{22}\text{Ne}$	$M(^{56}\text{Ni})_{t=0}$ (M_{\odot})	$M(^{58}\text{Ni})_{t=1 \text{ yr}}$ (M_{\odot})	$M(\text{Ni}_{\text{stable}})_{t=1 \text{ yr}}$ (M_{\odot})	Reference
(1)	(2)	(3)	(4)	(5)	(6)	(7)	(8)
M0.90_zne22_z0	2D	0.95	0.500 / 0.500 / 0.0	0.026	6.86 (−5)	6.49 (−4)	Kobayashi et al. (2020)
M0.90_zne22_z0p002	2D	0.95	0.499 / 0.499 / 2.0 (−3)	0.024	1.49 (−4)	7.30 (−4)	Kobayashi et al. (2020)
M0.90_zne22_z0p01	2D	0.95	0.495 / 0.495 / 1.0 (−2)	0.018	4.52 (−4)	1.04 (−3)	Kobayashi et al. (2020)
M0.90_zne22_z0p02	2D	0.95	0.490 / 0.490 / 2.0 (−2)	0.015	7.73 (−4)	1.37 (−3)	Kobayashi et al. (2020)
M0.90_zne22_z0p04	2D	0.95	0.480 / 0.480 / 4.0 (−2)	0.013	1.08 (−3)	1.72 (−3)	Kobayashi et al. (2020)
M1.00_zne22_z0	2D	1.05	0.500 / 0.500 / 0.0	0.642	9.63 (−4)	8.98 (−3)	Kobayashi et al. (2020)
M1.00_zne22_z0p002	2D	1.05	0.499 / 0.499 / 2.0 (−3)	0.638	1.19 (−3)	9.78 (−3)	Kobayashi et al. (2020)
M1.00_zne22_z0p01	2D	1.05	0.495 / 0.495 / 1.0 (−2)	0.620	1.11 (−2)	1.95 (−2)	Kobayashi et al. (2020)
M1.00_zne22_z0p02	2D	1.05	0.490 / 0.490 / 2.0 (−2)	0.600	2.50 (−2)	3.31 (−2)	Kobayashi et al. (2020)
M1.00_zne22_z0p04	2D	1.05	0.480 / 0.480 / 4.0 (−2)	0.564	5.36 (−2)	6.11 (−2)	Kobayashi et al. (2020)
M1.10_zne22_z0	2D	1.15	0.500 / 0.500 / 0.0	0.861	1.13 (−3)	1.13 (−2)	Kobayashi et al. (2020)
M1.10_zne22_z0p002	2D	1.15	0.499 / 0.499 / 2.0 (−3)	0.856	2.07 (−3)	1.29 (−2)	Kobayashi et al. (2020)
M1.10_zne22_z0p01	2D	1.15	0.495 / 0.495 / 1.0 (−2)	0.835	1.62 (−2)	2.66 (−2)	Kobayashi et al. (2020)
M1.10_zne22_z0p02	2D	1.15	0.490 / 0.490 / 2.0 (−2)	0.817	3.61 (−2)	4.58 (−2)	Kobayashi et al. (2020)
M1.10_zne22_z0p04	2D	1.15	0.480 / 0.480 / 4.0 (−2)	0.751	7.44 (−2)	8.32 (−2)	Kobayashi et al. (2020)
M1.20_zne22_z0	2D	1.25	0.500 / 0.500 / 0.0	1.053	5.16 (−3)	1.55 (−2)	Kobayashi et al. (2020)
M1.20_zne22_z0p002	2D	1.25	0.499 / 0.499 / 2.0 (−3)	1.048	7.08 (−3)	1.78 (−2)	Kobayashi et al. (2020)
M1.20_zne22_z0p01	2D	1.25	0.495 / 0.495 / 1.0 (−2)	1.025	2.36 (−2)	3.37 (−2)	Kobayashi et al. (2020)
M1.20_zne22_z0p02	2D	1.25	0.490 / 0.490 / 2.0 (−2)	0.995	4.53 (−2)	5.45 (−2)	Kobayashi et al. (2020)
M1.20_zne22_z0p04	2D	1.25	0.480 / 0.480 / 4.0 (−2)	0.937	8.44 (−2)	9.26 (−2)	Kobayashi et al. (2020)
ddet_sml4_d2e5	2D	1.02	0.400 / 0.580 / 2.0 (−2)	0.598	1.14 (−2)	2.55 (−2)	Townsley et al. (2019)
det_ONe10e7	2D	1.18	0.030 / 0.600 / 0.0 ^b	0.832	1.89 (−3)	3.49 (−3)	Marquardt et al. (2015)
det_ONe13e7	2D	1.21	0.030 / 0.600 / 0.0 ^b	0.941	2.81 (−3)	2.81 (−3)	Marquardt et al. (2015)
det_ONe15e7	2D	1.23	0.030 / 0.600 / 0.0 ^b	0.957	3.26 (−3)	5.12 (−3)	Marquardt et al. (2015)
det_ONe17e7	2D	1.24	0.030 / 0.600 / 0.0 ^b	0.990	3.74 (−3)	5.64 (−3)	Marquardt et al. (2015)
det_ONe20e7	2D	1.25	0.030 / 0.600 / 0.0 ^b	1.030	4.43 (−3)	6.36 (−3)	Marquardt et al. (2015)
<i>Violent WD Mergers</i>							
09+09	3D	1.73	0.500 / 0.500 / 0.0	0.124	2.90 (−5)	2.96 (−5)	Pakmor et al. (2010)
11+09	3D	1.94	0.475 / 0.500 / 2.5 (−2)	0.614	2.84 (−2)	3.03 (−2)	Pakmor et al. (2012)
09+076_Z1	3D	1.61	0.482 / 0.500 / 1.3 (−2)	0.183	1.60 (−3)	2.18 (−3)	Kromer et al. (2013)
09+076_Z0.01	3D	1.61	0.500 / 0.500 / 1.3 (−4)	0.197	6.63 (−5)	8.53 (−5)	Kromer et al. (2016)
<i>WD-WD Collisions</i>							
0.5-0.5	2D	1.00	0.493 / 0.493 / 1.5 (−2)	0.171	2.60 (−3)	2.60 (−3)	Kushnir (2021, priv. comm.)
0.6-0.6	2D	1.20	0.493 / 0.493 / 1.5 (−2)	0.378	6.20 (−3)	6.20 (−3)	Kushnir (2021, priv. comm.)
0.7-0.7	2D	1.40	0.493 / 0.493 / 1.5 (−2)	0.620	1.16 (−2)	1.16 (−2)	Kushnir (2021, priv. comm.)
0.8-0.8	2D	1.60	0.493 / 0.493 / 1.5 (−2)	0.723	1.46 (−2)	1.46 (−2)	Kushnir (2021, priv. comm.)
0.9-0.9	2D	1.80	0.493 / 0.493 / 1.5 (−2)	0.779	1.21 (−2)	1.21 (−2)	Kushnir (2021, priv. comm.)
1.0-1.0	2D	2.00	0.493 / 0.493 / 1.5 (−2)	1.206	3.68 (−2)	3.68 (−2)	Kushnir (2021, priv. comm.)

Note: Numbers in parentheses correspond to powers of ten.

^a We were not able to confirm the exact ^{22}Ne abundance in the solar-scaled composition models of Kobayashi et al. (2020).

^b The oxygen-neon WDs considered in the Marquardt et al. (2015) study have the following initial composition: $X(^{12}\text{C}) = 0.03$, $X(^{16}\text{O}) = 0.6$, and $X(^{20}\text{Ne}) = 0.37$. Since $X(^{22}\text{Ne}) = 0$, these models are considered to be at zero metallicity.

Appendix B: Atomic data for [Ni II] transitions

In Table B.1 we give the atomic data for the optical 7378 Å and NIR 1.94 μm [Ni II] transitions used in our CMFGEN calculations.

Appendix C: Modifying the Ni II/Ni III ratio in CMFGEN

In CMFGEN, the population density n_l (in cm^{-3}) of any given state (level) l is determined via a solution to the time-dependent statistical equilibrium equations (Hillier & Dessart 2012). The population density of the ionization state $i+$ ($i = 0$ for neutral, $i = 1$ for once-ionized etc.) for some species is then simply the sum of n_l over all N levels of that ionization state:

$$n^{i+} = \sum_{l=1}^N n_l^{i+}. \quad (\text{C.1})$$

We then define the Ni II/Ni III ratio as:

$$I_{23} = \frac{n^+}{n^{2+}}. \quad (\text{C.2})$$

In Sect. 4 we artificially modify the Ni II/Ni III ratio to test the impact on the resulting [Ni II] lines in late-time SN Ia spectra. At any given depth in the ejecta (denoted by index j , which corresponds to a given radius or velocity coordinate in our 1D spatial grid), we scale all the Ni II and Ni III level population densities by a factor of $a_{1,j}$ and $a_{2,j}$, respectively, to obtain new population densities:

$$\tilde{n}_j^+ = \sum_{l=1}^N a_{1,j} n_{l,j}^+ = a_{1,j} n_j^+ \quad (\text{C.3})$$

and

$$\tilde{n}_j^{2+} = \sum_{l=1}^N a_{2,j} n_{l,j}^{2+} = a_{2,j} n_j^{2+} \quad (\text{C.4})$$

in order to achieve a new Ni II/Ni III ratio \tilde{I}_{23} related to the original ratio I_{23} by some pre-determined factor:

$$\mathcal{R}_{23} = \frac{\tilde{I}_{23}}{I_{23}} = \frac{\tilde{n}_j^+}{\tilde{n}_j^{2+}} \frac{n_j^{2+}}{n_j^+} = \frac{a_{1,j}}{a_{2,j}}. \quad (\text{C.5})$$

Since we wish to preserve the total species population density at each depth, we further require that:

$$\tilde{n}_j^+ + \tilde{n}_j^{2+} = n_j^+ + n_j^{2+}, \quad (\text{C.6})$$

from which we derive an equation for the scale factor for the Ni III population density:

$$a_{2,j} = \frac{n_j^+(1 - a_{1,j}) + n_j^{2+}}{n_j^{2+}}, \quad (\text{C.7})$$

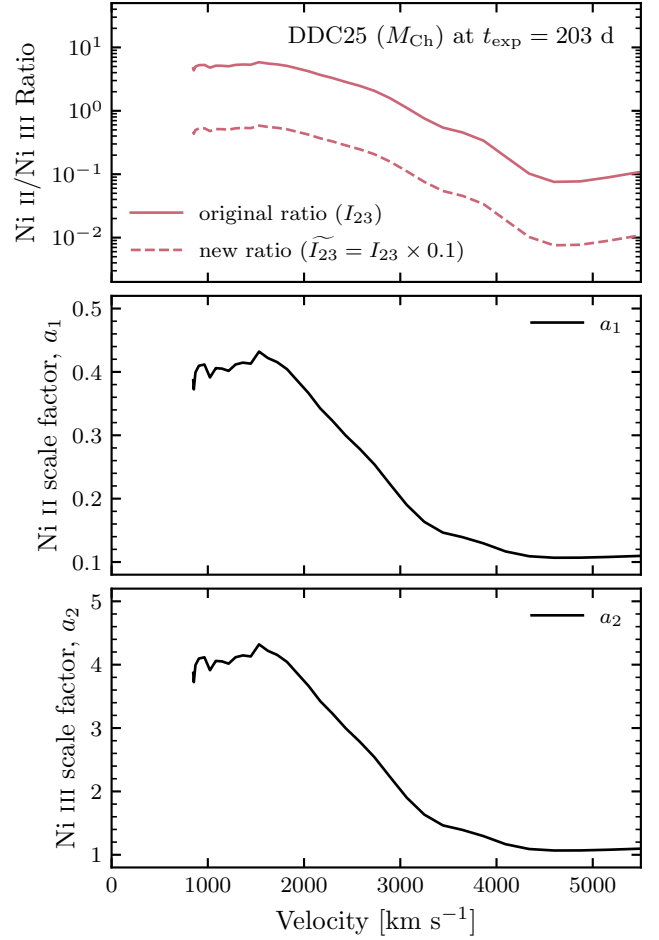


Fig. C.1. Illustration of the procedure used to modify the Ni II/Ni III ratio in CMFGEN. In this example we wish to scale the Ni II/Ni III ratio of the M_{Ch} model DDC25 at 203 d past explosion by $\mathcal{R}_{23} = 0.1$. The upper panel shows the original and scaled Ni II/Ni III ratios (Eq. C.2). The middle and bottom panels show the scaling coefficients (a_1, a_2) applied to the population densities of Ni II and Ni III, respectively (Eqs. C.8 and C.7). We note that $a_1/a_2 = \mathcal{R}_{23} = 0.1$ at all depths by definition (Eq. C.5). When the original Ni II/Ni III ratio becomes small enough ($\lesssim 10^{-1}$ beyond $\sim 4000 \text{ km s}^{-1}$), $a_1 \approx 0.1 (= \mathcal{R}_{23})$ and $a_2 \approx 1$, as expected (see text for details).

which we then plug into Eq. C.5 to derive the scale factor for the Ni II population density:

$$a_{1,j} = \frac{(n_j^+ + n_j^{2+}) \mathcal{R}_{23}}{n_j^+ \mathcal{R}_{23} + n_j^{2+}}, \quad (\text{C.8})$$

from which we trivially compute $a_{2,j} = a_{1,j} \mathcal{R}_{23}$ using Eq. C.5 (or Eq. C.7). When $n_j^+ \ll n_j^{2+}$ and $\mathcal{R}_{23} < 1$, $a_{1,j} \approx \mathcal{R}_{23}$ and $a_{2,j} \approx 1$, as seen in Fig. C.1.

The scaled Ni II and Ni III population densities are used as an input for an observer-frame calculation of the spectrum.

Table B.1. Forbidden [Ni II] transitions used in our CMFGEN simulations. The data were obtained from [Quinet & Le Dourneuf \(1996\)](#).

λ_{air} (Å)	Lower Level		Upper Level		Oscillator strength f	Einstein coefficient A_{ul} (s ⁻¹)
	Configuration	Index l	Configuration	Index u		
7377.829	3d ⁹ 2D _e [5/2]	1	3d ⁸ (3F)4s 2F _e [7/2]	7	2.1719×10^{-9}	1.9950×10^{-1}
19387.744	3d ⁸ (3F)4s 4F _e [9/2]	3	3d ⁸ (3F)4s 2F _e [7/2]	7	4.1701×10^{-9}	9.2450×10^{-2}